

Measurement of the Top Quark Mass using Template Methods on Dilepton Events in $p\bar{p}$ Collisions at $\sqrt{s} = 1.96$ TeV

A. Abulencia,²³ D. Acosta,¹⁷ J. Adelman,¹³ T. Affolder,¹⁰ T. Akimoto,⁵⁵ M.G. Albrow,¹⁶
D. Ambrose,¹⁶ S. Amerio,⁴³ D. Amidei,³⁴ A. Anastassov,⁵² K. Anikeev,¹⁶ A. Annovi,¹⁸
J. Antos,¹ M. Aoki,⁵⁵ G. Apollinari,¹⁶ J.-F. Arguin,³³ T. Arisawa,⁵⁷ A. Artikov,¹⁴
W. Ashmanskas,¹⁶ A. Attal,⁸ F. Azfar,⁴² P. Azzi-Bacchetta,⁴³ P. Azzurri,⁴⁶ N. Bacchetta,⁴³
H. Bachacou,²⁸ W. Badgett,¹⁶ A. Barbaro-Galtieri,²⁸ V.E. Barnes,⁴⁸ B.A. Barnett,²⁴
S. Baroiant,⁷ V. Bartsch,³⁰ G. Bauer,³² F. Bedeschi,⁴⁶ S. Behari,²⁴ S. Belforte,⁵⁴
G. Bellettini,⁴⁶ J. Bellinger,⁵⁹ A. Belloni,³² E. Ben Haim,⁴⁴ D. Benjamin,¹⁵ A. Beretvas,¹⁶
J. Beringer,²⁸ T. Berry,²⁹ A. Bhatti,⁵⁰ M. Binkley,¹⁶ D. Bisello,⁴³ R. E. Blair,² C. Blocker,⁶
B. Blumenfeld,²⁴ A. Bocci,¹⁵ A. Bodek,⁴⁹ V. Boisvert,⁴⁹ G. Bolla,⁴⁸ A. Bolshov,³²
D. Bortoletto,⁴⁸ J. Boudreau,⁴⁷ A. Boveia,¹⁰ B. Brau,¹⁰ C. Bromberg,³⁵ E. Brubaker,¹³
J. Budagov,¹⁴ H.S. Budd,⁴⁹ S. Budd,²³ K. Burkett,¹⁶ G. Busetto,⁴³ P. Bussey,²⁰
K. L. Byrum,² S. Cabrera,¹⁵ M. Campanelli,¹⁹ M. Campbell,³⁴ F. Canelli,⁸ A. Canepa,⁴⁸
D. Carlsmith,⁵⁹ R. Carosi,⁴⁶ S. Carron,¹⁵ M. Casarsa,⁵⁴ A. Castro,⁵ P. Catastini,⁴⁶
D. Cauz,⁵⁴ M. Cavalli-Sforza,³ A. Cerri,²⁸ L. Cerrito,⁴² S.H. Chang,²⁷ J. Chapman,³⁴
Y.C. Chen,¹ M. Chertok,⁷ G. Chiarelli,⁴⁶ G. Chlachidze,¹⁴ F. Chlebana,¹⁶ I. Cho,²⁷
K. Cho,²⁷ D. Chokheli,¹⁴ J.P. Chou,²¹ P.H. Chu,²³ S.H. Chuang,⁵⁹ K. Chung,¹²
W.H. Chung,⁵⁹ Y.S. Chung,⁴⁹ M. Ciljak,⁴⁶ C.I. Ciobanu,²³ M.A. Ciocci,⁴⁶ A. Clark,¹⁹
D. Clark,⁶ M. Coca,¹⁵ G. Compostella,⁴³ M.E. Convery,⁵⁰ J. Conway,⁷ B. Cooper,³⁰
K. Copic,³⁴ M. Cordelli,¹⁸ G. Cortiana,⁴³ F. Cresciolo,⁴⁶ A. Cruz,¹⁷ C. Cuenca Almenar,⁷
J. Cuevas,¹¹ R. Culbertson,¹⁶ D. Cyr,⁵⁹ S. DaRonco,⁴³ S. D'Auria,²⁰ M. D'Onofrio,³
D. Dagenhart,⁶ P. de Barbaro,⁴⁹ S. De Cecco,⁵¹ A. Deisher,²⁸ G. De Lentdecker,⁴⁹
M. Dell'Orso,⁴⁶ F. Delli Paoli,⁴³ S. Demers,⁴⁹ L. Demortier,⁵⁰ J. Deng,¹⁵ M. Deninno,⁵
D. De Pedis,⁵¹ P.F. Derwent,¹⁶ C. Dionisi,⁵¹ J.R. Dittmann,⁴ P. DiTuro,⁵² C. Dörr,²⁵
S. Donati,⁴⁶ M. Donega,¹⁹ P. Dong,⁸ J. Donini,⁴³ T. Dorigo,⁴³ S. Dube,⁵² K. Ebina,⁵⁷
J. Efron,³⁹ J. Ehlers,¹⁹ R. Erbacher,⁷ D. Errede,²³ S. Errede,²³ R. Eusebi,¹⁶ H.C. Fang,²⁸
S. Farrington,²⁹ I. Fedorko,⁴⁶ W.T. Fedorko,¹³ R.G. Feild,⁶⁰ M. Feindt,²⁵ J.P. Fernandez,³¹
R. Field,¹⁷ G. Flanagan,⁴⁸ L.R. Flores-Castillo,⁴⁷ A. Foland,²¹ S. Forrester,⁷ G.W. Foster,¹⁶
M. Franklin,²¹ J.C. Freeman,²⁸ I. Furic,¹³ M. Gallinaro,⁵⁰ J. Galyardt,¹² J.E. Garcia,⁴⁶

M. Garcia Sciveres,²⁸ A.F. Garfinkel,⁴⁸ C. Gay,⁶⁰ H. Gerberich,²³ D. Gerdes,³⁴ S. Giagu,⁵¹
P. Giannetti,⁴⁶ A. Gibson,²⁸ K. Gibson,¹² C. Ginsburg,¹⁶ N. Giokaris,¹⁴ K. Giolo,⁴⁸
M. Giordani,⁵⁴ P. Giromini,¹⁸ M. Giunta,⁴⁶ G. Giurgiu,¹² V. Glagolev,¹⁴ D. Glenzinski,¹⁶
M. Gold,³⁷ N. Goldschmidt,³⁴ J. Goldstein,⁴² G. Gomez,¹¹ G. Gomez-Ceballos,¹¹
M. Goncharov,⁵³ O. González,³¹ I. Gorelov,³⁷ A.T. Goshaw,¹⁵ Y. Gotra,⁴⁷ K. Goulianos,⁵⁰
A. Gresele,⁴³ M. Griffiths,²⁹ S. Grinstein,²¹ C. Grosso-Pilcher,¹³ R.C. Group,¹⁷
U. Grundler,²³ J. Guimaraes da Costa,²¹ Z. Gunay-Unalan,³⁵ C. Haber,²⁸ S.R. Hahn,¹⁶
K. Hahn,⁴⁵ E. Halkiadakis,⁵² A. Hamilton,³³ B.-Y. Han,⁴⁹ J.Y. Han,⁴⁹ R. Handler,⁵⁹
F. Happacher,¹⁸ K. Hara,⁵⁵ M. Hare,⁵⁶ S. Harper,⁴² R.F. Harr,⁵⁸ R.M. Harris,¹⁶
K. Hatakeyama,⁵⁰ J. Hauser,⁸ C. Hays,¹⁵ A. Heijboer,⁴⁵ B. Heinemann,²⁹ J. Heinrich,⁴⁵
M. Herndon,⁵⁹ D. Hidas,¹⁵ C.S. Hill,¹⁰ D. Hirschbuehl,²⁵ A. Hocker,¹⁶ A. Holloway,²¹
S. Hou,¹ M. Houlden,²⁹ S.-C. Hsu,⁹ B.T. Huffman,⁴² R.E. Hughes,³⁹ J. Huston,³⁵
J. Incandela,¹⁰ G. Introzzi,⁴⁶ M. Iori,⁵¹ Y. Ishizawa,⁵⁵ A. Ivanov,⁷ B. Iyutin,³² E. James,¹⁶
D. Jang,⁵² B. Jayatilaka,³⁴ D. Jeans,⁵¹ H. Jensen,¹⁶ E.J. Jeon,²⁷ S. Jindariani,¹⁷
M. Jones,⁴⁸ K.K. Joo,²⁷ S.Y. Jun,¹² T.R. Junk,²³ T. Kamon,⁵³ J. Kang,³⁴ P.E. Karchin,⁵⁸
Y. Kato,⁴¹ Y. Kemp,²⁵ R. Kephart,¹⁶ U. Kerzel,²⁵ V. Khotilovich,⁵³ B. Kilminster,³⁹
D.H. Kim,²⁷ H.S. Kim,²⁷ J.E. Kim,²⁷ M.J. Kim,¹² S.B. Kim,²⁷ S.H. Kim,⁵⁵ Y.K. Kim,¹³
L. Kirsch,⁶ S. Klimenko,¹⁷ M. Klute,³² B. Knuteson,³² B.R. Ko,¹⁵ H. Kobayashi,⁵⁵
K. Kondo,⁵⁷ D.J. Kong,²⁷ J. Konigsberg,¹⁷ K. Kordas,¹⁸ A. Korytov,¹⁷ A.V. Kotwal,¹⁵
A. Kovalev,⁴⁵ A. Kraan,⁴⁵ J. Kraus,²³ I. Kravchenko,³² M. Kreps,²⁵ J. Kroll,⁴⁵
N. Krumnack,⁴ M. Kruse,¹⁵ V. Krutelyov,⁵³ S. E. Kuhlmann,² Y. Kusakabe,⁵⁷ S. Kwang,¹³
A.T. Laasanen,⁴⁸ S. Lai,³³ S. Lami,⁴⁶ S. Lammel,¹⁶ M. Lancaster,³⁰ R.L. Lander,⁷
K. Lannon,³⁹ A. Lath,⁵² G. Latino,⁴⁶ I. Lazzizzera,⁴³ T. LeCompte,² J. Lee,⁴⁹ J. Lee,²⁷
Y.J. Lee,²⁷ S.W. Lee,⁵³ R. Lefèvre,³ N. Leonardo,³² S. Leone,⁴⁶ S. Levy,¹³ J.D. Lewis,¹⁶
C. Lin,⁶⁰ C.S. Lin,¹⁶ M. Lindgren,¹⁶ E. Lipeles,⁹ A. Lister,¹⁹ D.O. Litvintsev,¹⁶ T. Liu,¹⁶
N.S. Lockyer,⁴⁵ A. Loginov,³⁶ M. Loretì,⁴³ P. Loverre,⁵¹ R.-S. Lu,¹ D. Lucchesi,⁴³
P. Lujan,²⁸ P. Lukens,¹⁶ G. Lungu,¹⁷ L. Lyons,⁴² J. Lys,²⁸ R. Lysak,¹ E. Lytken,⁴⁸
P. Mack,²⁵ D. MacQueen,³³ R. Madrak,¹⁶ K. Maeshima,¹⁶ T. Maki,²² P. Maksimovic,²⁴
S. Malde,⁴² G. Manca,²⁹ F. Margaroli,⁵ R. Marginean,¹⁶ C. Marino,²³ A. Martin,⁶⁰
V. Martin,³⁸ M. Martínez,³ T. Maruyama,⁵⁵ H. Matsunaga,⁵⁵ M.E. Mattson,⁵⁸ R. Mazini,³³

P. Mazzanti,⁵ K.S. McFarland,⁴⁹ P. McIntyre,⁵³ R. McNulty,²⁹ A. Mehta,²⁹ S. Menzemer,¹¹
 A. Menzione,⁴⁶ P. Merkel,⁴⁸ C. Mesropian,⁵⁰ A. Messina,⁵¹ M. von der Mey,⁸ T. Miao,¹⁶
 N. Miladinovic,⁶ J. Miles,³² R. Miller,³⁵ J.S. Miller,³⁴ C. Mills,¹⁰ M. Milnik,²⁵
 R. Miquel,²⁸ A. Mitra,¹ G. Mitselmakher,¹⁷ A. Miyamoto,²⁶ N. Moggi,⁵ B. Mohr,⁸
 R. Moore,¹⁶ M. Morello,⁴⁶ P. Movilla Fernandez,²⁸ J. Mülmenstädt,²⁸ A. Mukherjee,¹⁶
 Th. Muller,²⁵ R. Mumford,²⁴ P. Murat,¹⁶ J. Nachtman,¹⁶ J. Naganoma,⁵⁷ S. Nahn,³²
 I. Nakano,⁴⁰ A. Napier,⁵⁶ D. Naumov,³⁷ V. Necula,¹⁷ C. Neu,⁴⁵ M.S. Neubauer,⁹
 J. Nielsen,²⁸ T. Nigmanov,⁴⁷ L. Nodulman,² O. Norriella,³ E. Nurse,³⁰ T. Ogawa,⁵⁷
 S.H. Oh,¹⁵ Y.D. Oh,²⁷ T. Okusawa,⁴¹ R. Oldeman,²⁹ R. Orava,²² K. Osterberg,²²
 C. Pagliarone,⁴⁶ E. Palencia,¹¹ R. Paoletti,⁴⁶ V. Papadimitriou,¹⁶ A.A. Paramonov,¹³
 B. Parks,³⁹ S. Pashapour,³³ J. Patrick,¹⁶ G. Pauletta,⁵⁴ M. Paulini,¹² C. Paus,³²
 D.E. Pellett,⁷ A. Penzo,⁵⁴ T.J. Phillips,¹⁵ G. Piacentino,⁴⁶ J. Piedra,⁴⁴ L. Pinera,¹⁷
 K. Pitts,²³ C. Plager,⁸ L. Pondrom,⁵⁹ X. Portell,³ O. Poukhov,¹⁴ N. Pounder,⁴²
 F. Prakoshyn,¹⁴ A. Pronko,¹⁶ J. Proudfoot,² F. Ptohos,¹⁸ G. Punzi,⁴⁶ J. Pursley,²⁴
 J. Rademacker,⁴² A. Rahaman,⁴⁷ A. Rakitin,³² S. Rappoccio,²¹ F. Ratnikov,⁵² B. Reisert,¹⁶
 V. Rekovic,³⁷ N. van Remortel,²² P. Renton,⁴² M. Rescigno,⁵¹ S. Richter,²⁵ F. Rimondi,⁵
 L. Ristori,⁴⁶ W.J. Robertson,¹⁵ A. Robson,²⁰ T. Rodrigo,¹¹ E. Rogers,²³ S. Rolli,⁵⁶
 R. Roser,¹⁶ M. Rossi,⁵⁴ R. Rossin,¹⁷ C. Rott,⁴⁸ A. Ruiz,¹¹ J. Russ,¹² V. Rusu,¹³
 H. Saarikko,²² S. Sabik,³³ A. Safonov,⁵³ W.K. Sakumoto,⁴⁹ G. Salamanna,⁵¹ O. Saltó,³
 D. Saltzberg,⁸ C. Sanchez,³ L. Santi,⁵⁴ S. Sarkar,⁵¹ L. Sartori,⁴⁶ K. Sato,⁵⁵ P. Savard,³³
 A. Savoy-Navarro,⁴⁴ T. Scheidle,²⁵ P. Schlabach,¹⁶ E.E. Schmidt,¹⁶ M.P. Schmidt,⁶⁰
 M. Schmitt,³⁸ T. Schwarz,³⁴ L. Scodellaro,¹¹ A.L. Scott,¹⁰ A. Scribano,⁴⁶ F. Scuri,⁴⁶
 A. Sedov,⁴⁸ S. Seidel,³⁷ Y. Seiya,⁴¹ A. Semenov,¹⁴ L. Sexton-Kennedy,¹⁶ I. Sfiligoi,¹⁸
 M.D. Shapiro,²⁸ T. Shears,²⁹ P.F. Shepard,⁴⁷ D. Sherman,²¹ M. Shimojima,⁵⁵
 M. Shochet,¹³ Y. Shon,⁵⁹ I. Shreyber,³⁶ A. Sidoti,⁴⁴ P. Sinervo,³³ A. Sisakyan,¹⁴ J. Sjolín,⁴²
 A. Skiba,²⁵ A.J. Slaughter,¹⁶ K. Sliwa,⁵⁶ J.R. Smith,⁷ F.D. Snider,¹⁶ R. Snihur,³³
 M. Soderberg,³⁴ A. Soha,⁷ S. Somalwar,⁵² V. Sorin,³⁵ J. Spalding,¹⁶ M. Spezziga,¹⁶
 F. Spinella,⁴⁶ T. Spreitzer,³³ P. Squillacioti,⁴⁶ M. Stanitzki,⁶⁰ A. Staveris-Polykalas,⁴⁶
 R. St. Denis,²⁰ B. Stelzer,⁸ O. Stelzer-Chilton,⁴² D. Stentz,³⁸ J. Strologas,³⁷ D. Stuart,¹⁰
 J.S. Suh,²⁷ A. Sukhanov,¹⁷ K. Sumorok,³² H. Sun,⁵⁶ K. Sung,³³ I. Suslov,¹⁴

T. Suzuki,⁵⁵ A. Taffard,²³ R. Takashima,⁴⁰ Y. Takeuchi,⁵⁵ K. Takikawa,⁵⁵ M. Tanaka,²
R. Tanaka,⁴⁰ N. Tanimoto,⁴⁰ M. Tecchio,³⁴ P.K. Teng,¹ K. Terashi,⁵⁰ S. Tether,³²
J. Thom,¹⁶ A.S. Thompson,²⁰ E. Thomson,⁴⁵ P. Tipton,⁴⁹ V. Tiwari,¹² S. Tkaczyk,¹⁶
D. Toback,⁵³ S. Tokar,¹⁴ K. Tollefson,³⁵ T. Tomura,⁵⁵ D. Tonelli,⁴⁶ M. Tönnesmann,³⁵
S. Torre,¹⁸ D. Torretta,¹⁶ S. Tourneur,⁴⁴ W. Trischuk,³³ R. Tsuchiya,⁵⁷ S. Tsuno,⁴⁰
N. Turini,⁴⁶ F. Ukegawa,⁵⁵ T. Unverhau,²⁰ S. Uozumi,⁵⁵ D. Usynin,⁴⁵ A. Vaiciulis,⁴⁹
S. Vallecorsa,¹⁹ A. Varganov,³⁴ E. Vataga,³⁷ G. Velev,¹⁶ G. Veramendi,²³ V. Veszpremi,⁴⁸
R. Vidal,¹⁶ I. Vila,¹¹ R. Vilar,¹¹ T. Vine,³⁰ I. Vollrath,³³ I. Volobouev,²⁸ G. Volpi,⁴⁶
F. Würthwein,⁹ P. Wagner,⁵³ R. G. Wagner,² R.L. Wagner,¹⁶ W. Wagner,²⁵ R. Wallny,⁸
T. Walter,²⁵ Z. Wan,⁵² S.M. Wang,¹ A. Warburton,³³ S. Waschke,²⁰ D. Waters,³⁰
W.C. Wester III,¹⁶ B. Whitehouse,⁵⁶ D. Whiteson,⁴⁵ A.B. Wicklund,² E. Wicklund,¹⁶
G. Williams,³³ H.H. Williams,⁴⁵ P. Wilson,¹⁶ B.L. Winer,³⁹ P. Wittich,¹⁶ S. Wolbers,¹⁶
C. Wolfe,¹³ T. Wright,³⁴ X. Wu,¹⁹ S.M. Wynne,²⁹ A. Yagil,¹⁶ K. Yamamoto,⁴¹
J. Yamaoka,⁵² T. Yamashita,⁴⁰ C. Yang,⁶⁰ U.K. Yang,¹³ Y.C. Yang,²⁷ W.M. Yao,²⁸
G.P. Yeh,¹⁶ J. Yoh,¹⁶ K. Yorita,¹³ T. Yoshida,⁴¹ G.B. Yu,⁴⁹ I. Yu,²⁷ S.S. Yu,¹⁶ J.C. Yun,¹⁶
L. Zanello,⁵¹ A. Zanetti,⁵⁴ I. Zaw,²¹ F. Zetti,⁴⁶ X. Zhang,²³ J. Zhou,⁵² and S. Zucchelli⁵

(CDF Collaboration)

¹*Institute of Physics, Academia Sinica,*

Taipei, Taiwan 11529, Republic of China

²*Argonne National Laboratory, Argonne, Illinois 60439*

³*Institut de Fisica d'Altes Energies,*

Universitat Autònoma de Barcelona,

E-08193, Bellaterra (Barcelona), Spain

⁴*Baylor University, Waco, Texas 76798*

⁵*Istituto Nazionale di Fisica Nucleare,*

University of Bologna, I-40127 Bologna, Italy

⁶*Brandeis University, Waltham, Massachusetts 02254*

⁷*University of California, Davis, Davis, California 95616*

⁸*University of California, Los Angeles, Los Angeles, California 90024*

⁹*University of California, San Diego, La Jolla, California 92093*

- ¹⁰*University of California, Santa Barbara, Santa Barbara, California 93106*
- ¹¹*Instituto de Fisica de Cantabria, CSIC-University of Cantabria, 39005 Santander, Spain*
- ¹²*Carnegie Mellon University, Pittsburgh, PA 15213*
- ¹³*Enrico Fermi Institute, University of Chicago, Chicago, Illinois 60637*
- ¹⁴*Joint Institute for Nuclear Research, RU-141980 Dubna, Russia*
- ¹⁵*Duke University, Durham, North Carolina 27708*
- ¹⁶*Fermi National Accelerator Laboratory, Batavia, Illinois 60510*
- ¹⁷*University of Florida, Gainesville, Florida 32611*
- ¹⁸*Laboratori Nazionali di Frascati, Istituto Nazionale
di Fisica Nucleare, I-00044 Frascati, Italy*
- ¹⁹*University of Geneva, CH-1211 Geneva 4, Switzerland*
- ²⁰*Glasgow University, Glasgow G12 8QQ, United Kingdom*
- ²¹*Harvard University, Cambridge, Massachusetts 02138*
- ²²*Division of High Energy Physics, Department of Physics,
University of Helsinki and Helsinki Institute of Physics, FIN-00014, Helsinki, Finland*
- ²³*University of Illinois, Urbana, Illinois 61801*
- ²⁴*The Johns Hopkins University, Baltimore, Maryland 21218*
- ²⁵*Institut für Experimentelle Kernphysik,
Universität Karlsruhe, 76128 Karlsruhe, Germany*
- ²⁶*High Energy Accelerator Research Organization (KEK), Tsukuba, Ibaraki 305, Japan*
- ²⁷*Center for High Energy Physics: Kyungpook National University,
Taegu 702-701; Seoul National University,
Seoul 151-742; and SungKyunKwan University, Suwon 440-746; Korea*
- ²⁸*Ernest Orlando Lawrence Berkeley National Laboratory, Berkeley, California 94720*
- ²⁹*University of Liverpool, Liverpool L69 7ZE, United Kingdom*
- ³⁰*University College London, London WC1E 6BT, United Kingdom*
- ³¹*Centro de Investigaciones Energeticas
Medioambientales y Tecnologicas, E-28040 Madrid, Spain*
- ³²*Massachusetts Institute of Technology, Cambridge, Massachusetts 02139*
- ³³*Institute of Particle Physics: McGill University, Montréal,
Canada H3A 2T8; and University of Toronto, Toronto, Canada M5S 1A7*
- ³⁴*University of Michigan, Ann Arbor, Michigan 48109*

- ³⁵*Michigan State University, East Lansing, Michigan 48824*
- ³⁶*Institution for Theoretical and Experimental Physics, ITEP, Moscow 117259, Russia*
- ³⁷*University of New Mexico, Albuquerque, New Mexico 87131*
- ³⁸*Northwestern University, Evanston, Illinois 60208*
- ³⁹*The Ohio State University, Columbus, Ohio 43210*
- ⁴⁰*Okayama University, Okayama 700-8530, Japan*
- ⁴¹*Osaka City University, Osaka 588, Japan*
- ⁴²*University of Oxford, Oxford OX1 3RH, United Kingdom*
- ⁴³*University of Padova, Istituto Nazionale di Fisica Nucleare,
Sezione di Padova-Trento, I-35131 Padova, Italy*
- ⁴⁴*LPNHE-Universite de Paris 6/IN2P3-CNRS*
- ⁴⁵*University of Pennsylvania, Philadelphia, Pennsylvania 19104*
- ⁴⁶*Istituto Nazionale di Fisica Nucleare Pisa, Universities of Pisa,
Siena and Scuola Normale Superiore, I-56127 Pisa, Italy*
- ⁴⁷*University of Pittsburgh, Pittsburgh, Pennsylvania 15260*
- ⁴⁸*Purdue University, West Lafayette, Indiana 47907*
- ⁴⁹*University of Rochester, Rochester, New York 14627*
- ⁵⁰*The Rockefeller University, New York, New York 10021*
- ⁵¹*Istituto Nazionale di Fisica Nucleare, Sezione di Roma 1,
University of Rome “La Sapienza,” I-00185 Roma, Italy*
- ⁵²*Rutgers University, Piscataway, New Jersey 08855*
- ⁵³*Texas A&M University, College Station, Texas 77843*
- ⁵⁴*Istituto Nazionale di Fisica Nucleare, University of Trieste/ Udine, Italy*
- ⁵⁵*University of Tsukuba, Tsukuba, Ibaraki 305, Japan*
- ⁵⁶*Tufts University, Medford, Massachusetts 02155*
- ⁵⁷*Waseda University, Tokyo 169, Japan*
- ⁵⁸*Wayne State University, Detroit, Michigan 48201*
- ⁵⁹*University of Wisconsin, Madison, Wisconsin 53706*
- ⁶⁰*Yale University, New Haven, Connecticut 06520*

(Dated: August 22, 2018)

Abstract

We describe a measurement of the top quark mass from events produced in $p\bar{p}$ collisions at a center-of-mass energy of 1.96 TeV, using the Collider Detector at Fermilab. We identify $t\bar{t}$ candidates where both W bosons from the top quarks decay into leptons ($e\nu$, $\mu\nu$, or $\tau\nu$) from a data sample of 360 pb^{-1} . The top quark mass is reconstructed in each event separately by three different methods, which draw upon simulated distributions of the neutrino pseudorapidity, $t\bar{t}$ longitudinal momentum, or neutrino azimuthal angle in order to extract probability distributions for the top quark mass. For each method, representative mass distributions, or templates, are constructed from simulated samples of signal and background events, and parameterized to form continuous probability density functions. A likelihood fit incorporating these parameterized templates is then performed on the data sample masses in order to derive a final top quark mass. Combining the three template methods, taking into account correlations in their statistical and systematic uncertainties, results in a top quark mass measurement of $170.1 \pm 6.0 \text{ (stat.)} \pm 4.1 \text{ (syst.) GeV}/c^2$.

PACS numbers: 14.65Ha, 13.85.Qk, 13.85.Ni

I. INTRODUCTION

The top quark, the weak isospin partner of the bottom quark, was first observed by the CDF and DØ collaborations in $p\bar{p}$ collisions produced at the Fermilab Tevatron [1]. During Run I operation from 1992 to 1995, CDF acquired 109 pb^{-1} of data at a center-of-mass energy of 1.8 TeV, and performed the first measurements of top quark properties. Since the start of Run II at the Tevatron in 2001, CDF has collected integrated luminosities several times that of Run I. Increased top production from a higher collision energy and improved acceptance of the upgraded detector have further enhanced the Run II top quark yield. This larger sample size allows for more precise studies of the characteristics of the top quark.

As with all quarks, the top quark mass is not predicted by theory, and therefore represents a free parameter in the standard model which must be experimentally determined. Tevatron Run I measurements yielded a top quark mass of $178.0 \pm 4.3 \text{ GeV}/c^2$ [2], approximately 40 times heavier than the next heaviest quark, the bottom quark. Such a large mass, close to the electroweak symmetry breaking scale $v = (\sqrt{2}G_F)^{-1/2} \approx 246 \text{ GeV}$, suggests that the top quark may play a special role in this process [3]. The subsequently large contribution to quark-loop corrections of electroweak parameters from the heavy top quark provides for powerful tests of the standard model. In particular, a precise measurement of the top quark mass, coupled with that of the W boson, leads to tighter constraints on the as yet unobserved Higgs boson [4].

At the Tevatron, in $p\bar{p}$ collisions with a center-of-mass energy of 1.96 TeV, top quarks are produced mainly in $t\bar{t}$ pairs, through $q\bar{q}$ annihilation ($\sim 85\%$) and gluon-gluon fusion. Because of its large width and correspondingly short lifetime ($\sim 10^{-25} \text{ s}$), the top quark decays before any hadronization can take place, so that its existence as a “free quark” can be studied without the complication of lower energy QCD effects. In the framework of the standard model, each top quark decays almost exclusively to an on-shell W boson and a bottom quark. The b quark subsequently hadronizes into a jet of particles, while the W decays either to a $q\bar{q}'$ or a lepton-neutrino pair. Thus, the decays of the W bosons determine the characteristics of a $t\bar{t}$ event and, consequently, the event selection strategy.

The “all hadronic” mode, where both W 's decay into $q\bar{q}'$ pairs, occurs for $\sim 44\%$ of $t\bar{t}$ events, but this topology is dominated by a large QCD multijet background. The most precise top quark mass measurements arise from the “lepton+jets” mode ($\sim 30\%$ of events),

where one W decays hadronically while the other decays to either an electron or muon plus a neutrino, whose presence can be inferred from missing transverse energy in the detector. A third mode occurs when both W bosons from each top quark decay into leptons ($e\nu$, $\mu\nu$, or $\tau\nu$). Though this “dilepton” mode accounts for only $\sim 11\%$ of $t\bar{t}$ events, such measurements are important in order to reduce the overall uncertainty on the top quark mass. Further, dilepton measurements test the consistency of top quark mass results obtained using other decay modes, as the dilepton mode contains different background sources and, therefore, represents an inherently different event sample. Since all top quark mass measurements assume a sample composition of $t\bar{t}$ and standard model background events, any discrepancy among the measured top masses could indicate the presence of new physics processes.

This paper reports a measurement of the top quark mass with the CDF II detector by combining three analysis methods for the dilepton channel. Each analysis selects candidate $t\bar{t}$ dilepton decays using one of two complementary event selection strategies, which differ in lepton identification criteria and subsequent signal-to-background ratios. In each analysis a single, representative top quark mass for each event is reconstructed using different kinematical assumptions in order to constrain the $t\bar{t}$ dilepton decay. The distributions of reconstructed top quark masses obtained from the data are compared with simulated mass distributions (templates) for signal and background events, and likelihood fits are used to arrive at a final top quark mass for each analysis technique. Accounting for correlations in statistical and systematic uncertainties, the results of the three analyses are then combined to determine the top quark mass in the dilepton channel using template methods.

II. DETECTOR AND EVENT SELECTION

The data sample used for these analyses was collected by the Collider Detector at Fermilab [5] during Run II operation between March 2002 and August 2004. As depicted in Fig. 1, the CDF II detector is an azimuthally and forward-backward symmetric apparatus designed to study $p\bar{p}$ reactions at the Tevatron. We use a cylindrical coordinate system about the proton beam axis in which θ is the polar angle, ϕ is the azimuthal angle, and pseudorapidity is defined as $\eta \equiv -\ln[\tan(\theta/2)]$. The detector has a charged particle tracking system immersed in a 1.4 T magnetic field, aligned coaxially with the $p\bar{p}$ beams. The Run II Silicon Vertex Detector (SVX II) and Intermediate Silicon Layer (ISL) provide tracking over the radial range 1.5 to 28 cm [6]. A 3.1 m long open-cell drift chamber, the Central Outer Tracker (COT), covers the radial range from 40 to 137 cm [7]. The fiducial region of the silicon detector extends to pseudorapidity $|\eta| \sim 2$, while the COT provides coverage for $|\eta| \lesssim 1$.

Segmented electromagnetic and hadronic sampling calorimeters surround the tracking system and measure the energy flow of interacting particles in the pseudorapidity range $|\eta| < 3.6$. This analysis uses the new end plug detectors [8] to identify electron candidates with $1.2 < |\eta| < 2.0$ in addition to the central detectors [9] for lepton candidates with $|\eta| < 1.1$. A set of drift chambers and scintillation counters [10] located outside the central hadron calorimeters and another set behind a 60 cm iron shield detect muon candidates with $|\eta| \lesssim 0.6$. Additional chambers and counters detect muons in the region $0.6 \leq |\eta| \leq 1.0$. Gas Cherenkov counters [11] located in the $3.7 < |\eta| < 4.7$ region measure the average number of inelastic $p\bar{p}$ collisions per bunch crossing and thereby determine the beam luminosity.

The signature of $t\bar{t}$ decays in the dilepton channel is two jets from the b quarks, two high-momentum leptons and large missing energy (due to the unobserved neutrinos) from the W decays, and the possibility of extra jets from initial or final-state radiation. The major backgrounds for dilepton $t\bar{t}$ events are from Drell-Yan dilepton production ($q\bar{q} \rightarrow Z/\gamma^* \rightarrow e^+e^-, \mu^+\mu^-, \tau^+\tau^-$), $W(\rightarrow \ell\nu)$ +jets events where a jet “fakes” the signature of the second lepton, and diboson production (WW, WZ, ZZ).

The data are derived from inclusive lepton triggers demanding central electrons with transverse energy $E_T \equiv E \sin \theta > 18$ GeV, or central muons with transverse momentum $p_T \equiv p \sin \theta > 18$ GeV/ c . Electrons in the end plug are required to have $E_T > 20$ GeV.

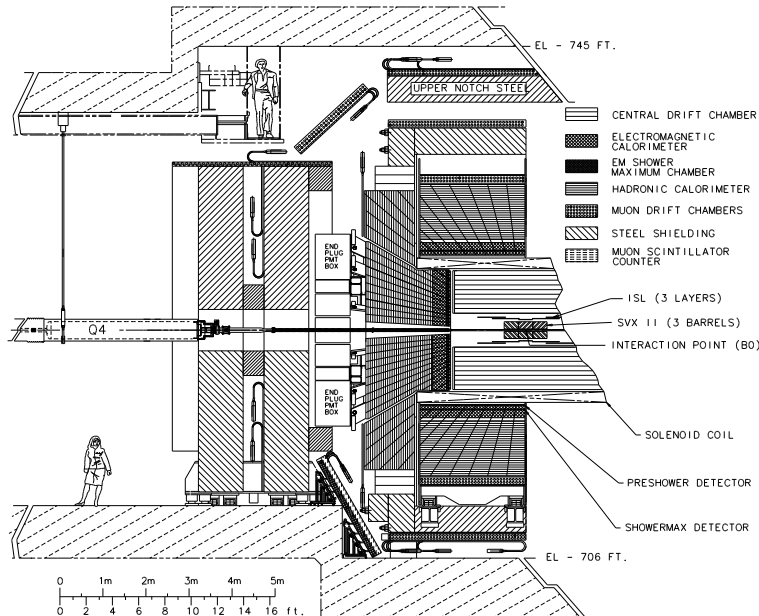


FIG. 1: Elevation view of the CDF II detector, showing the inner silicon microstrip detector, Central Outer Tracker drift chamber, electromagnetic and hadronic calorimeters, and muon drift chambers and scintillation counters.

Events must also have a missing transverse energy $\cancel{E}_T > 15$ GeV, calculated from the vector sum $-\sum_i E_T^i \vec{n}_i$, where \vec{n}_i is the unit vector in the azimuthal plane which points from the beam line to the i^{th} calorimeter tower.

The top quark mass analyses described here employ one of two sets of selection criteria developed for the $t\bar{t}$ cross section measurement in the dilepton decay channel [12]. The first method, referred to as the “dilepton” (DIL) analysis, is similar to that used in the CDF Run I measurement [13], and requires both candidate leptons to be specifically identified as either electrons or muons. A second “lepton+track” (LTRK) method increases the efficiency of the event selection (at the cost of a larger background) by requiring one well-identified lepton (electron or muon) in conjunction with an isolated track with large transverse momentum. This method recovers events where leptons fall in calorimeter or muon detector gaps, and increases the acceptance for single prong hadronic decays of the τ lepton from $W \rightarrow \tau\nu$ (approximately 20% of the total LTRK acceptance, compared with 12% for the DIL selection).

Both selection methods demand a “tight” lepton in combination with a “loose” lepton of

opposite charge. Requirements for the tight lepton are identical for both methods, but differ for the loose lepton. Tight leptons must have well-measured tracks, based on the numbers of silicon and drift chamber hits and reconstructed vertex position, and have $E_T > 20$ GeV. Tight leptons must also satisfy the isolation requirement that the total calorimeter E_T within a cone $\Delta R \equiv \sqrt{\Delta\eta^2 + \Delta\phi^2} = 0.4$ about the lepton trajectory not exceed 10% of the lepton's E_T . Tight electrons must have lateral and longitudinal electromagnetic shower profiles in the calorimeter consistent with electrons, while tight muons must point to muon chamber hits and have a calorimeter signature compatible with minimum-ionizing particles. For the DIL method, loose leptons must be well-identified electrons or muons with no isolation requirement. Loose DIL electrons must be central, while the muon chamber hit requirements for loose DIL muons are relaxed. Loose leptons in the LTRK method, in contrast, are simply required to be well-measured and isolated tracks within $|\eta| < 1$ and having $p_T > 20$ GeV/ c . The LTRK loose lepton isolation is determined from the p_T sum of neighboring tracks within the cone $\Delta R = 0.4$ about the lepton track, which must not exceed 10% that of the lepton.

At least two jets are required per event, and are derived from looking for clusters of energy in calorimeter towers within a cone size of $\Delta R = 0.4$. This total jet E_T is corrected for non-uniformities in the response of the calorimeter as a function of η , effects from multiple $p\bar{p}$ collisions, and the hadronic jet energy scale of the calorimeter [14]. Jets are required to have $|\eta| < 2.5$ and $E_T > 15$ GeV for the DIL analysis, or $|\eta| < 2.0$ and $E_T > 20$ GeV for the LTRK method. The two highest E_T jets for each event are assumed to stem from the b quarks; this assumption is true for $\sim 70\%$ of simulated $t\bar{t}$ events. For application in the top quark mass measurements, these jets are further corrected for energy deposited from the underlying $p\bar{p}$ event or lost outside the search cone $\Delta R = 0.4$. The momentum components of each b quark are then calculated from the measured jet E_T and angle by assuming a b quark mass of 5.0 GeV/ c^2 . No explicit identification of b jets is used.

The final signature of a dilepton $t\bar{t}$ event is missing transverse energy \cancel{E}_T in the calorimeter. For calorimeter tower clusters associated with an identified jet, the \cancel{E}_T vector sum uses the transverse jet energy which has been corrected for calorimeter response and multiple $p\bar{p}$ collision effects. The \cancel{E}_T for events with an identified muon is further corrected by the measured muon momentum. Dilepton $t\bar{t}$ events must satisfy the requirement $\cancel{E}_T > 25$ GeV. False \cancel{E}_T may arise through mismeasurement of the leptons or jets. Therefore, both DIL and LTRK methods require a minimum angular separation $\Delta\phi$ between lepton or jet trajectories

and the \cancel{E}_T vector. For the DIL selection, events must have $\Delta\phi > 20^\circ$ for all leptons and jets if $\cancel{E}_T < 50$ GeV. In the LTRK method, the \cancel{E}_T vector cannot be within 5° of either the tight lepton direction or the axis of the loose lepton, and jets must have $\Delta\phi > 25^\circ$ for events with $\cancel{E}_T < 50$ GeV.

The dominant source of background for both selection methods is from Drell-Yan ($q\bar{q} \rightarrow Z/\gamma^* \rightarrow ee, \mu\mu$) events. These events should have no real \cancel{E}_T , and can only satisfy the selection criteria if there is mismeasurement of the lepton or jet E_T . Therefore, additional selection requirements are imposed for events where the reconstructed invariant mass of the two lepton candidates lies within $15 \text{ GeV}/c^2$ of the Z boson resonance. For these events, the DIL method requires a “jet significance” of > 8 , defined as the ratio of \cancel{E}_T to the sum of jet E_T projected along the \cancel{E}_T direction. The LTRK method increases the \cancel{E}_T requirement to $\cancel{E}_T > 40$ GeV for dilepton events near the Z resonance. The DIL method further suppresses background processes by requiring that the scalar sum of jet E_T , lepton p_T , and \cancel{E}_T (denoted by H_T) exceed 200 GeV.

Table I summarizes the luminosity and expected numbers of signal and background events for the DIL and LTRK selection methods, along with observed results from the inclusive lepton data set. The LTRK selection comprises a 6% greater luminosity since it is able to accept $e\mu$ dilepton decays when muon detectors were not operational. The acceptance and efficiency of $t\bar{t}$ signal events are calculated with a full detector simulation using PYTHIA [15] Monte Carlo and assuming a production cross section of 6.1 pb, corresponding to a top mass of $178 \text{ GeV}/c^2$ [16]. The Drell-Yan, $W(\rightarrow \ell\nu)$ +jets fakes, and diboson background acceptances are estimated using a combination of Drell-Yan and W +jets data, and PYTHIA and ALPGEN+HERWIG [17, 18] simulation. The total uncertainties for expected event yields include both the statistical uncertainties of the Monte Carlo samples used, as well as systematic uncertainties from particle identification, jet energy measurement, and modeling of the $t\bar{t}$ signal and background. Applied to the inclusive lepton data set, the DIL selection observes 33 events, and the LTRK selection observes 46 events, representing upward fluctuations for both selections from the predicted numbers of events at the assumed $t\bar{t}$ cross section. The DIL and LTRK data samples share 24 events in common, leading to a union of 55 events with a 44% overlap.

TABLE I: Luminosity, expected $t\bar{t}$ signal and background (with total uncertainties), and observed number of events for the DIL and LTRK selection methods. A $t\bar{t}$ cross section of 6.1 pb is assumed, corresponding to a top mass of 178 GeV/ c^2 .

	DIL	LTRK
Luminosity	340 pb ⁻¹	360 pb ⁻¹
Expected $t\bar{t}$	15.7 ± 1.3	19.4 ± 1.4
Drell-Yan	5.5 ± 1.2	8.7 ± 3.3
$W(\rightarrow \ell\nu)$ +jets fakes	3.5 ± 1.4	4.0 ± 1.2
Diboson	1.6 ± 0.3	2.0 ± 0.4
Total background	10.5 ± 1.9	14.7 ± 3.6
Total expected	26.2 ± 2.3	34.1 ± 3.9
Observed	33	46

III. METHODS FOR TOP MASS MEASUREMENT

Reconstruction of the top quark mass from dilepton events involves an underconstrained system. For lepton+jets decays, the two components of \cancel{E}_T generated by the single neutrino, along with other assumptions about the $t\bar{t}$ event (*e.g.*, equal masses for the t and \bar{t} quarks, and invariant masses of the $\ell\nu$ and $q\bar{q}'$ systems equal to the W mass) are enough to allow a kinematically overconstrained fit. For dilepton $t\bar{t}$ events, in contrast, the measured \cancel{E}_T is due to two neutrinos, so that the decay assumptions are insufficient to constrain the event.

Specifically, for each $t\bar{t}$ event, the kinematics are fully specified by 24 quantities: the four-momenta of the six final state particles. Twelve three-momentum components of the two b -quarks and two leptons are measured by the detector, along with the two components of \cancel{E}_T . The four mass values of the final state b -quarks and leptons are known, while the two neutrinos are assumed to be massless. Making three additional assumptions about the $t\bar{t}$ and W boson decays:

$$m(b\ell^+\nu) = m(\bar{b}\ell^-\bar{\nu}) \tag{1}$$

$$m(\ell^+\nu) = m(W^+) \tag{2}$$

$$m(\ell^-\bar{\nu}) = m(W^-) \tag{3}$$

results in only 23 measured, known, or assumed components of the system. Therefore, the top quark mass cannot be directly reconstructed from $t\bar{t}$ dilepton decays, but requires one additional kinematic assumption to constrain the system.

In practice, for each event we integrate over undetermined kinematical variables to obtain distributions giving the relative likelihood of different values of the top quark mass. The three mass analyses are distinguished by different choices of kinematical variable, different methods for determining the likelihood of each top quark mass, and different approaches to distilling the resulting information into one top quark mass per event. This section describes each technique in turn. We model the $t\bar{t}$ decay kinematics and optimize each method over a large range of top quark masses, using HERWIG Monte Carlo simulation with CTEQ5L [19] parton distribution functions. Potential biases in the reconstructed top quark masses are taken into account in the comparison of the measured distributions with top quark mass templates derived using the same simulation, as discussed in Section IV.

A. Neutrino Weighting Algorithm (NWA)

One method for estimating the top quark mass from dilepton events uses the Neutrino Weighting Algorithm (NWA). In Run I at the Tevatron, the NWA method was one of two techniques used by DØ [20], and was employed by CDF [21] to measure the top quark mass. The method therefore provides a baseline for CDF Run II measurements, and is applied to the 360 pb⁻¹ LTRK event sample. The strategy of the algorithm is to solve for the neutrino and antineutrino momenta, independently of the measured missing energy, by making additional assumptions about the $t\bar{t}$ decay. The neutrino/antineutrino solutions are then compared with the measured \cancel{E}_T through a weight function in order to create a probability distribution for the event as a function of top quark mass.

The NWA weight function is constructed as follows. We assume values for the top quark and W boson masses, the pseudorapidities of the neutrino and antineutrino, and the lepton-jet pairings associated with the top/antitop decays. We apply energy-momentum conservation to the top quark decay and obtain up to two possible solutions for the 4-momentum (ν) of the neutrino. We repeat this procedure on the antitop decay, resulting in up to four possible pairs of neutrino-antineutrino solutions ($\nu, \bar{\nu}$). Each of the four solutions is assigned a probability (weight, w_i) that it describes the observed missing transverse energy components \cancel{E}_x and \cancel{E}_y within their uncertainties σ_x and σ_y , respectively:

$$w_i = \exp\left(-\frac{(\cancel{E}_x - p_x^\nu - p_x^{\bar{\nu}})^2}{2\sigma_x^2}\right) \cdot \exp\left(-\frac{(\cancel{E}_y - p_y^\nu - p_y^{\bar{\nu}})^2}{2\sigma_y^2}\right). \quad (4)$$

We use $\sigma_x = \sigma_y = 15$ GeV, which is obtained from $t\bar{t}$ Monte Carlo simulation generated with $m_t = 178$ GeV/ c^2 . In practice, however, the performance of the algorithm is insensitive to the particular choice of \cancel{E}_T resolution.

Given the assumed top quark mass and assumed neutrino η values, any of the four solution pairs ($\nu, \bar{\nu}$) have *a priori* equal probability. We therefore sum the four weights:

$$w(m_t, \eta_\nu, \eta_{\bar{\nu}}, \ell\text{-jet}) = \sum_{i=1}^4 w_i. \quad (5)$$

Not knowing which are the true neutrino η 's in our event, we repeat the above steps for many possible $(\eta_\nu, \eta_{\bar{\nu}})$ pairs. As seen in the upper plots of Fig. 2, Monte Carlo $t\bar{t}$ simulation indicates that the neutrino η 's are uncorrelated, and follow a Gaussian distribution centered at zero with a width near one. Since the neutrino η width varies little with top quark mass

(as shown in the lower plot of Fig. 2), we assume a constant width for all top quark masses corresponding to the value of 0.988 obtained from the $m_t = 178 \text{ GeV}/c^2$ sample. To ensure symmetry and smoothness, we scan the neutrino η distributions from -3 to $+3$ in steps of 0.1, and each $(\eta_\nu, \eta_{\bar{\nu}})$ pair is assigned a probability of occurrence $P(\eta_\nu, \eta_{\bar{\nu}})$ derived from a Gaussian of width 0.988. Each trial $(\eta_\nu, \eta_{\bar{\nu}})$ pair contributes to the event according to its weight (Eq. 5) and probability of occurrence, $P(\eta_\nu, \eta_{\bar{\nu}})$:

$$w(m_t, \ell - jet) = \sum_{\eta_\nu, \eta_{\bar{\nu}}} P(\eta_\nu, \eta_{\bar{\nu}}) \cdot w(m_t, \eta_\nu, \eta_{\bar{\nu}}, \ell - jet). \quad (6)$$

Since we do not distinguish b jets from \bar{b} jets, both possible lepton-jet pairings are summed. Thus, the final weight becomes a function only of the top quark mass, after integrating over all other unknowns:

$$W(m_t) = \sum_{\ell^+ - jet_1}^{\ell^+ - jet_2} w(m_t, \ell - jet). \quad (7)$$

We scan m_t from 80 to 380 GeV/c^2 in steps of 1 GeV/c^2 . Figure 3 shows the resulting normalized weight distribution from Eq. 7 after applying the NWA method to a HERWIG Monte Carlo $t\bar{t}$ event, with a simulated top quark mass of 170 GeV/c^2 . We choose one indicative top quark mass for each event, selecting the most probable value (MPV) of the weight distribution as that which best explains the event as a $t\bar{t}$ dilepton decay.

For a given event, there exists a small probability that the kinematics of the decay will fail to produce a solution for any scanned top quark mass. This efficiency for finding a solution is thus an additional event selection criterion. Studies of simulated $t\bar{t}$ dilepton events show that this NWA efficiency for signal is 99.8%, and independent of generated top quark mass. Applying the NWA method to Monte Carlo background samples shows that the efficiency for finding a kinematical solution varies between sources, ranging from 94-100%, with an average background efficiency of 96%.

B. Full Kinematic Analysis (KIN)

A second method for determining the top quark mass in the dilepton channel, called the Full Kinematic Analysis (KIN), is applied to the 340 pb^{-1} DIL selection sample. The KIN method resolves the underconstrained dilepton $t\bar{t}$ decays by introducing an additional

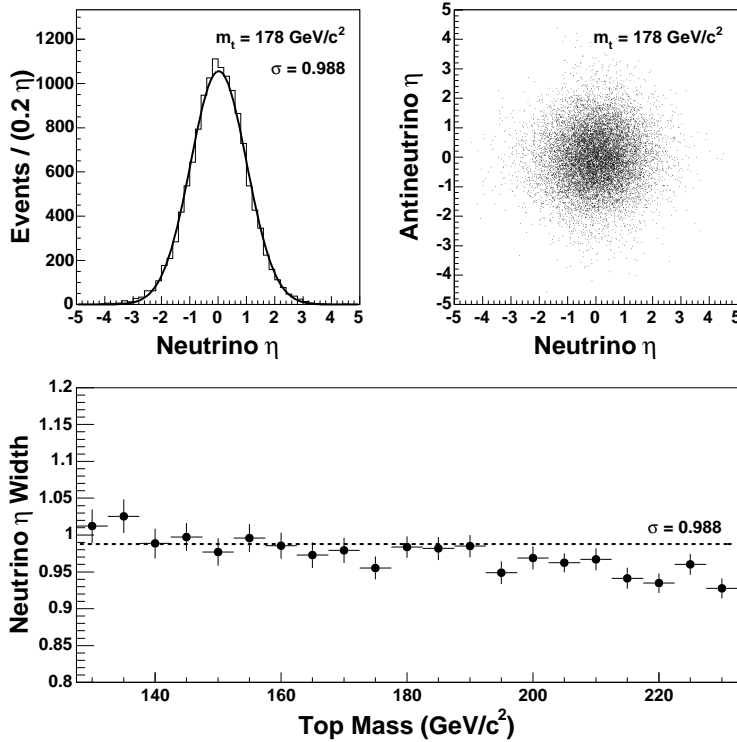


FIG. 2: Neutrino η distribution with Gaussian fit (upper left) and neutrino vs. antineutrino η (upper right) from a HERWIG $t\bar{t}$ sample with $m_t = 178 \text{ GeV}/c^2$. Lower plot shows η width as a function of generated top quark mass, compared with fit value at $m_t = 178 \text{ GeV}/c^2$ (horizontal line).

equation for the longitudinal momentum of the $t\bar{t}$ system, $p_z^{t\bar{t}}$. With the 6-particle final state constrained, the KIN method solves the resulting kinematic equations numerically to determine the top quark mass for each event.

Ideally, the quantity $p_z^{t\bar{t}}$ should be determined theoretically, and should be virtually independent of the top quark mass. Studies from Monte Carlo simulation over a range of top quark masses from 140-200 GeV/c^2 show that $p_z^{t\bar{t}}$ has a Gaussian behavior, with a mean of zero and a width near 180 GeV/c . This width increases by roughly 10% across the top quark mass range studied. The validity of our Monte Carlo simulation can be tested with data from lepton+jets $t\bar{t}$ events, where $p_z^{t\bar{t}}$ can be reconstructed explicitly. Figure 4 compares $p_z^{t\bar{t}}$ from the lepton+jets data sample with $t\bar{t}$ and background Monte Carlo samples, showing good agreement between data and simulation. The lepton+jets event selection, using secondary vertex b -quark identification, and subsequent backgrounds are similar to those of the

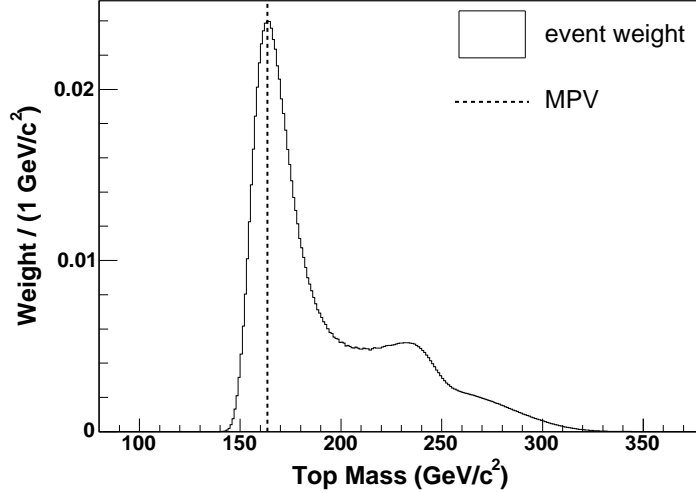


FIG. 3: NWA weight distribution as a function of top quark mass hypothesis (from Eq. 7) for a HERWIG Monte Carlo $t\bar{t}$ event with $m_t = 170 \text{ GeV}/c^2$. The vertical line denotes the most probable value (MPV) of m_t chosen by the method.

lepton+jets cross section measurement [22].

Using the measured momenta of the b -quarks and leptons, the two components of the measured \cancel{E}_T , and assumptions about the six final-state particle masses, the additional constraint on $p_z^{t\bar{t}}$, along with constraints on the W and $t\bar{t}$ decays, lead to the following set of kinematic equations:

$$\begin{aligned}
 p_x^\nu + p_x^{\bar{\nu}} &= \cancel{E}_x & (8) \\
 p_y^\nu + p_y^{\bar{\nu}} &= \cancel{E}_y \\
 p_z^t + p_z^{\bar{t}} &= 0 \pm 180 \text{ GeV}/c \\
 m_t &= m_{\bar{t}} \\
 m_{W^\pm} &= 80.4 \text{ GeV}/c^2 \\
 \vec{p}_b + \vec{p}_{W^+} &= \vec{p}_t \\
 \vec{p}_{\bar{b}} + \vec{p}_{W^-} &= \vec{p}_{\bar{t}} \\
 \vec{p}_{l^+} + \vec{p}_\nu &= \vec{p}_{W^+} \\
 \vec{p}_{l^-} + \vec{p}_{\bar{\nu}} &= \vec{p}_{W^-}.
 \end{aligned}$$

These equations have two solutions, which are determined through an iterative procedure.

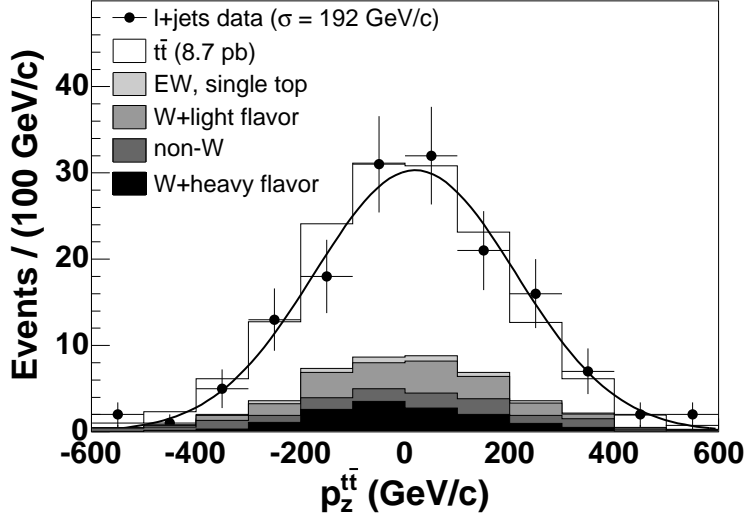


FIG. 4: Comparison of $t\bar{t}$ longitudinal momentum between lepton+jets data (with associated Gaussian fit) and standard model processes. The data corresponds to a sample of 318 pb^{-1} . The $t\bar{t}$ signal uses PYTHIA Monte Carlo with $m_t = 178 \text{ GeV}/c^2$, corresponding to a cross section of 8.7 pb .

If solutions cannot be found by using the above assumptions for the top and bottom quark masses, these requirements are relaxed, and we accept solutions where $m_{W^\pm} = 80.4 \pm 3.0 \text{ GeV}/c^2$ and $m_t = m_{\bar{t}} \pm 2.0 \text{ GeV}/c^2$. If no solutions are found after relaxing the mass requirements, the event is rejected.

The iterative procedure employed, Newton's Method [23], solves equations of the form $f(x)=0$. The method requires an initial guess for x which is reasonably close to the true root. The local derivative $f'(x)$ is then computed and extrapolated to zero, providing a better approximation for the root. This procedure is repeated according to:

$$x^{n+1} = x^n - \frac{f(x^n)}{f'(x^n)} \quad (9)$$

until a satisfactory solution is found. The method is extended to a system of k equations $F(\vec{x}) = f_i(\vec{x})$ by determining the $k \times k$ Jacobian matrix $J_F^{ij}(\vec{x}) = \frac{\partial f_i(\vec{x})}{\partial x_j}$, where $(i = 1, k; j = 1, k)$. In actuality, the method solves the linear equations:

$$J_F(\vec{x}^n) \cdot (\vec{x}^{n+1} - \vec{x}^n) = -F(\vec{x}^n) \quad (10)$$

for the unknown $\vec{x}^{n+1} - \vec{x}^n$, in order to avoid having to compute the inverse of $J_F(\vec{x}^n)$.

Applying Newton's Method to the $t\bar{t}$ decay system of Eq. 8, we determine the first of two pairs of quadratic solutions for the neutrino momentum according to the following set of three equations:

$$f_1(p_x^{\nu_1}, p_y^{\nu_1}, p_z^{\nu_1}) \equiv (E_{l_1} + E_{\nu_1})^2 - (\vec{p}_{l_1} + \vec{p}_{\nu_1})^2 - m_W^2 = 0 \quad (11)$$

$$f_2(p_x^{\nu_2}, p_y^{\nu_2}, p_z^{\nu_2}) \equiv (E_{l_2} + E_{\nu_2})^2 - (\vec{p}_{l_2} + \vec{p}_{\nu_2})^2 - m_W^2 = 0 \quad (12)$$

$$f_3(p_x^{\nu_1}, p_y^{\nu_1}, p_z^{\nu_1}) \equiv (E_{l_1} + E_{\nu_1} + E_{b_1})^2 - (\vec{p}_{l_1} + \vec{p}_{\nu_1} + \vec{p}_{b_1})^2 \\ - (E_{l_2} + E_{\nu_2} + E_{b_2})^2 + (\vec{p}_{l_2} + \vec{p}_{\nu_2} + \vec{p}_{b_2})^2 = 0 \quad (13)$$

from which the full kinematic chain is reconstructed, and the top quark mass solutions are calculated. The second quadratic solution for neutrino momentum $\vec{p}_{\nu_1}' \equiv \vec{p}_{\nu_1} + \vec{X}$ satisfies the following set of equations:

$$f_1(x_1, x_2, x_3) \equiv \sqrt{m_W^2 + (\vec{p}_{W_1} + \vec{X})^2} - E_{l_1} - \sqrt{(\vec{p}_{\nu_1} + \vec{X})^2} = 0 \quad (14)$$

$$f_2(x_1, x_2, x_3) \equiv \sqrt{m_W^2 + (\vec{p}_{W_2} - \vec{X})^2} - E_{l_2} - \sqrt{(\vec{p}_{\nu_2} - \vec{X})^2} = 0 \quad (15)$$

$$f_3(x_1, x_2, x_3) \equiv \sqrt{(\sqrt{m_W^2 + (\vec{p}_{W_1} + \vec{X})^2} + E_{b_1})^2 - (\vec{p}_{t_1} + \vec{X})^2} \\ - \sqrt{(\sqrt{m_W^2 + (\vec{p}_{W_2} - \vec{X})^2} + E_{b_2})^2 - (\vec{p}_{t_2} - \vec{X})^2} = 0 \quad (16)$$

from which a second pair of top quark mass solutions is found. Since there are two possible combinations of b -quark jets and leptons, we have a total of eight possible solutions for the top quark mass.

In order to incorporate the large range of possible $p_z^{t\bar{t}}$ values about the mean of zero (as seen in Fig. 4), as well as the finite resolutions of the measured momenta and \cancel{E}_T , the above procedure is repeated 10,000 times for each possible solution. For each repetition, the value of $p_z^{t\bar{t}}$ is drawn from a Gaussian distribution with zero mean and width of 180 GeV/ c . The jet energies and \cancel{E}_T are similarly smeared by Gaussians according to their estimated resolutions, while the relatively better resolutions on the measured jet angles and lepton momenta are assumed to be perfectly measured. Kinematic reconstruction of the smeared events results in a distribution of possible top quark masses for a given event (consistent with the measured kinematic characteristics of the event and the measurement uncertainties). The most probable value (MPV) of a spline fit to this mass distribution is then taken as the "raw top quark mass" for a given solution.

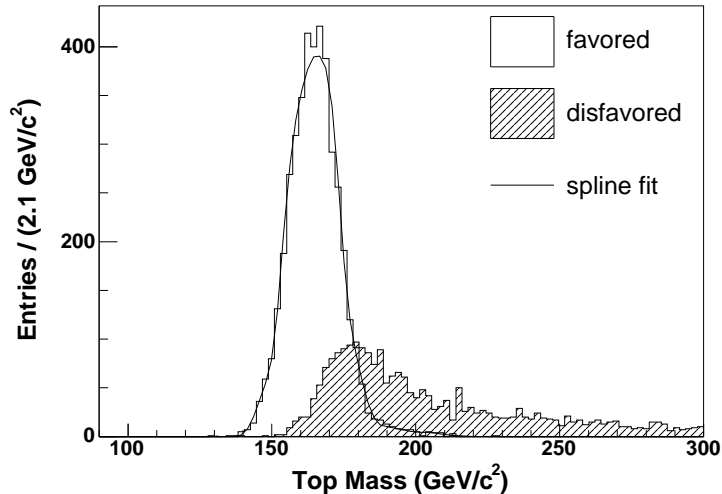


FIG. 5: Smeared top quark mass distributions of the “favored” and “disfavored” lepton-jet pairings from the KIN method applied to a HERWIG Monte Carlo $t\bar{t}$ event with $m_t = 170 \text{ GeV}/c^2$. Also shown for the “favored” pair is the spline fit used to select the top quark mass for a given solution.

The KIN method then selects a single “raw top quark mass” from the eight possible solutions as follows. Of the four possible solutions for each lepton-jet pairing, we choose that with the smallest effective mass of the $t\bar{t}$ system. Based on simulated events at $m_t = 178 \text{ GeV}/c^2$, this particular mass solution is closest to the generator-level top quark mass for approximately 84% of the events. The smeared mass distributions of the remaining two possible solutions (due to the two lepton-jet pairings) are then compared, as shown in Fig. 5 for an example simulation event. We choose the lepton-jet pair which produces the largest number of entries (*i.e.* fewest number of rejections) in the smeared distribution. The mass solution from this kinematically “favored” pair is found to be closest to the generated top quark mass for about 70% of events. In this manner, the KIN method returns a single top quark mass for each $t\bar{t}$ dilepton event. Although this method necessarily has a bias towards lower top masses, this bias is fully included in the simulation used to extract the final top mass value.

C. Neutrino ϕ Weighting Method (PHI)

A third procedure for analyzing $t\bar{t}$ dilepton decays, referred to as the Neutrino ϕ Weighting Method (PHI), most closely resembles the Run I lepton+jets template analysis [21]. Introducing additional assumptions about the azimuthal angle ϕ of the final-state neutrinos, this method reconstructs dilepton decays through the minimization of a chi-square functional (χ^2) to arrive at a single top quark mass for each event. As with the KIN analysis, the PHI method uses the 340 pb⁻¹ DIL selection sample.

The χ^2 functional to be minimized takes the form:

$$\chi^2 = \sum_{\ell=1}^2 \frac{(p_T^\ell - \widetilde{p}_T^\ell)^2}{\sigma_{p_T}^{\ell 2}} + \sum_{j=1}^2 \frac{(p_T^j - \widetilde{p}_T^j)^2}{\sigma_{p_T}^{j 2}} + \sum_{i=1}^N \frac{(UE^i - \widetilde{UE}^i)^2}{\sigma_{UE}^{i 2}} \quad (17)$$

$$+ \frac{(m_{\ell_1\nu_1} - m_W)^2}{\Gamma_W^2} + \frac{(m_{\ell_2\nu_2} - m_W)^2}{\Gamma_W^2} + \frac{(m_{j_1\ell_1\nu_1} - \widetilde{m}_t)^2}{\Gamma_t^2} + \frac{(m_{j_2\ell_2\nu_2} - \widetilde{m}_t)^2}{\Gamma_t^2}.$$

The first term sums over the primary lepton transverse momenta p_T^ℓ , with detector resolutions for the electrons and muons taken to be [5]:

$$\frac{\sigma_{p_T}^e}{p_T^e} = \sqrt{\frac{0.135^2}{p_T^e} + 0.02^2} \quad (18)$$

$$\frac{\sigma_{p_T}^\mu}{p_T^\mu} = 0.0011 \cdot p_T^\mu. \quad (19)$$

The second χ^2 term sums over the transverse momenta p_T^j of the two leading jets. These transverse momenta have been further corrected for underlying event and out-of-cone energy, and have a p_T and η -dependent detector resolution $\sigma_{p_T}^j$ derived from simulation. The quantity UE (with uncertainty σ_{UE}) in the third χ^2 term denotes the unclustered energy in the calorimeter, summed over ($i = 1, N$) towers, which is not associated with a lepton or leading jet calorimeter cluster, but includes any additional jets with $E_T > 8$ GeV/ c^2 and $|\eta| < 2.5$. The quantities $m_{\ell\nu}$ and $m_{j\ell\nu}$ in Eq. 17 refer to the reconstructed invariant masses of the W boson and top quark decay products, respectively. For the W boson decay width we use the P.D.G. value $\Gamma_W = 2.1$ GeV/ c^2 [24], while for the top quark we assume a width of $\Gamma_t = 2.5$ GeV/ c^2 . Variables with a tilde refer to the output of the minimization procedure. The quantity \widetilde{m}_t is the fit parameter returned as the reconstructed top quark mass for the combination being considered.

To resolve the neutrino momentum used in the W and top decay constraints of Eq. 17, two additional assumptions are needed. Assuming values for both neutrino azimuthal angles

$(\phi_{\nu 1}, \phi_{\nu 2})$, the transverse momenta of the neutrinos are linked through the measured \cancel{E}_T by:

$$\begin{aligned} p_T^{\nu 1} \cdot \cos(\phi_{\nu 1}) + p_T^{\nu 2} \cdot \cos(\phi_{\nu 2}) &= \cancel{E}_x \\ p_T^{\nu 1} \cdot \sin(\phi_{\nu 1}) + p_T^{\nu 2} \cdot \sin(\phi_{\nu 2}) &= \cancel{E}_y \end{aligned} \quad (20)$$

leading to the solutions:

$$\begin{aligned} p_x^{\nu 1} &\equiv p_T^{\nu 1} \cdot \cos(\phi_{\nu 1}) = \frac{\cancel{E}_x \cdot \sin(\phi_{\nu 2}) - \cancel{E}_y \cdot \cos(\phi_{\nu 2})}{\sin(\phi_{\nu 2} - \phi_{\nu 1})} \cdot \cos(\phi_{\nu 1}) \\ p_y^{\nu 1} &\equiv p_T^{\nu 1} \cdot \sin(\phi_{\nu 1}) = \frac{\cancel{E}_x \cdot \sin(\phi_{\nu 2}) - \cancel{E}_y \cdot \cos(\phi_{\nu 2})}{\sin(\phi_{\nu 2} - \phi_{\nu 1})} \cdot \sin(\phi_{\nu 1}) \\ p_x^{\nu 2} &\equiv p_T^{\nu 2} \cdot \cos(\phi_{\nu 2}) = \frac{\cancel{E}_x \cdot \sin(\phi_{\nu 1}) - \cancel{E}_y \cdot \cos(\phi_{\nu 1})}{\sin(\phi_{\nu 1} - \phi_{\nu 2})} \cdot \cos(\phi_{\nu 2}) \\ p_y^{\nu 2} &\equiv p_T^{\nu 2} \cdot \sin(\phi_{\nu 2}) = \frac{\cancel{E}_x \cdot \sin(\phi_{\nu 1}) - \cancel{E}_y \cdot \cos(\phi_{\nu 1})}{\sin(\phi_{\nu 1} - \phi_{\nu 2})} \cdot \sin(\phi_{\nu 2}). \end{aligned} \quad (21)$$

Performing the χ^2 minimization of Eq. 17 on all allowed values of neutrino ϕ creates a set of solutions in the $(\phi_{\nu 1}, \phi_{\nu 2})$ plane. In practice, only points in the quadrant $(0 < \phi_{\nu 1} < \pi, 0 < \phi_{\nu 2} < \pi)$ need to be sampled, since identical neutrino momentum components from Eq. 21 occur for the four points $(\phi_{\nu 1}, \phi_{\nu 2})$, $(\phi_{\nu 1} + \pi, \phi_{\nu 2})$, $(\phi_{\nu 1}, \phi_{\nu 2} + \pi)$, and $(\phi_{\nu 1} + \pi, \phi_{\nu 2} + \pi)$. Since $p_T^{\nu 1, \nu 2}$ must be positive by definition, and will only change sign by adding π to $\phi_{\nu 1, \nu 2}$, only one of the four points represents a physical solution. Solutions from other points are unphysical and can be interpreted as “mirror reflections” of the physical solution.

A grid of 12×12 points in the $(\phi_{\nu 1}, \phi_{\nu 2})$ plane is chosen, in a manner which avoids points where $\sin(\phi_{\nu 1} - \phi_{\nu 2}) = 0$ and Eq. 21 becomes undefined. At each point, 8 solutions exist due to the two-fold ambiguity in longitudinal momentum for each neutrino, and the two possible lepton-jet combinations. Thus, for each event, 1152 minimizations of Eq. 17 are performed, each returning an output χ^2 and reconstructed top quark mass m^{rec} . The minimal value for χ^2 among the 8 possible solutions at each point is retained, reducing each event to an array of 144 χ_{ij}^2 and m_{ij}^{rec} values, where $(i = 1, 12; j = 1, 12)$ refer to the $(\phi_{\nu 1}, \phi_{\nu 2})$ grid points. Each point is weighted by its returned χ^2 value according to:

$$w_{ij} = \frac{\exp(-\chi_{ij}^2/2)}{\sum_{i=1}^{12} \sum_{j=1}^{12} \exp(-\chi_{ij}^2/2)} \quad (22)$$

to create a probability density distribution normalized to unity.

To arrive at a single top quark mass value per event, the reconstructed mass values m_{ij}^{rec} of the array are averaged, using the weights derived from Eq. 22. The sensitivity to the top

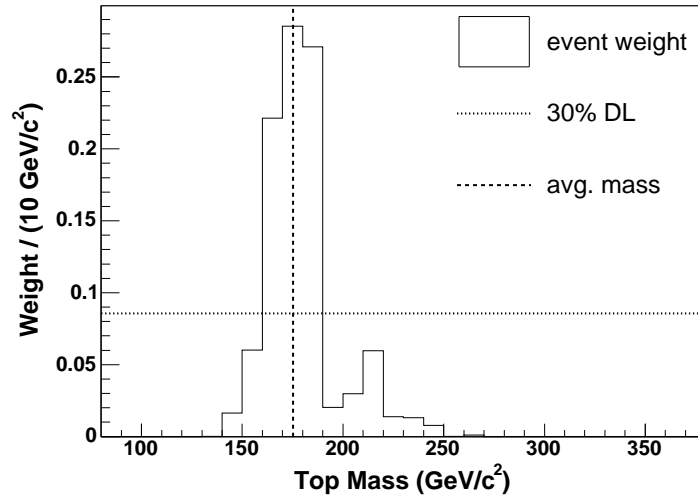


FIG. 6: Binned weight distribution from the PHI method for a HERWIG Monte Carlo $t\bar{t}$ event with $m_t = 170 \text{ GeV}/c^2$, showing the resulting average mass for bins above the 30% discrimination level (DL).

quark mass is enhanced by averaging only points with a weight at least 30% that of the most probable value in the probability density distribution. Figure 6 shows the results of the PHI method applied to a HERWIG Monte Carlo $t\bar{t}$ event with $m_t = 170 \text{ GeV}/c^2$.

IV. TEMPLATE LIKELIHOOD PROCEDURE

The three independent measurement techniques described in Section III produce a single top quark mass for each event in their corresponding data samples, which are mixtures of $t\bar{t}$ signal and background events. To arrive at a final top quark mass measurement, these data events are compared with probability density functions (p.d.f.'s) for signal and background within a likelihood minimization. The p.d.f.'s are developed from template mass distributions created by applying the NWA, KIN, and PHI methods to simulated $t\bar{t}$ signal and background samples, which are then parameterized. For the NWA and PHI methods, this parameterization uses a combination of Gaussian and gamma distribution terms. Similarly, the KIN method parameterization contains a Gaussian term in conjunction with an approximate Landau distribution.

A. Template construction

For the signal, we use $t\bar{t}$ dilepton events generated with HERWIG Monte Carlo simulation for top quark masses from 130 to 230 GeV/ c^2 in 5 GeV/ c^2 increments. The CTEQ5L [19] Structure Functions are used to model the momentum distribution of the initial state partons. For the NWA and PHI methods, the signal templates obtained from this simulation are parameterized as the sum of a Gaussian and a gamma distribution. This parameterization gives the signal p.d.f, $P_s(m; m_t)$, representing the probability of reconstructing a top quark mass m when the true mass is m_t :

$$P_s(m; m_t) = \alpha_5 \frac{\alpha_2^{1+\alpha_1}}{\Gamma(1 + \alpha_1)} (m - \alpha_0)^{\alpha_1} \exp(-\alpha_2(m - \alpha_0)) \quad (23)$$

$$+ (1 - \alpha_5) \frac{1}{\alpha_4 \sqrt{2\pi}} \exp\left(-\frac{(m - \alpha_3)^2}{2\alpha_4^2}\right).$$

The six parameters α_i in Eq. 23 are assumed to be linearly dependent on the generated top quark mass, such that we in fact perform a 12-parameter fit for p_i on all templates simultaneously, with:

$$\alpha_i = p_i + (m_t - 175 \text{ GeV}/c^2) p_{i+6}. \quad (24)$$

Figures 7 and 8 show representative signal templates from the NWA and PHI methods, with the corresponding parameterized fitting function.

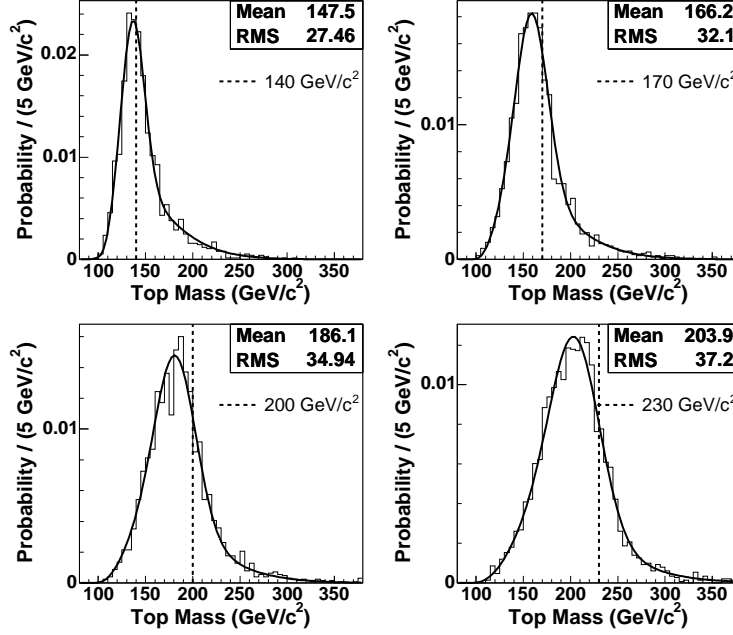


FIG. 7: Example signal templates as a function of the reconstructed top quark mass, from the NWA method applied to simulated signal samples at top quark masses of 130, 160, 190 and 220 GeV/c^2 . Overlaid are the parameterized fitting functions using Eq. 23. The vertical line indicates the generated top quark mass.

The signal template parameterization employed by the KIN method contains the Gaussian and Landau-like terms:

$$\lambda_{\text{Gauss}} = \frac{m - \alpha_4(m_t)}{\alpha_5(m_t)} \quad (25)$$

$$\lambda_{\text{Landau}} = \frac{m - \alpha_1(m_t)}{\alpha_2(m_t)} \quad (26)$$

which form the probability density function:

$$P_s(m; m_t) = \frac{\alpha_3(m_t)}{I_1} \exp(-0.5(\lambda_{\text{Landau}} + \exp(-\lambda_{\text{Landau}}))) + \frac{(1 - \alpha_3(m_t))}{I_2} \exp(-0.5\lambda_{\text{Gauss}}^2) \quad (27)$$

for reconstructing a top quark mass m given a true mass m_t . The Gaussian and Landau terms are normalized for solutions within the reconstructed mass range $90 < m < 300 \text{ GeV}/c^2$ by

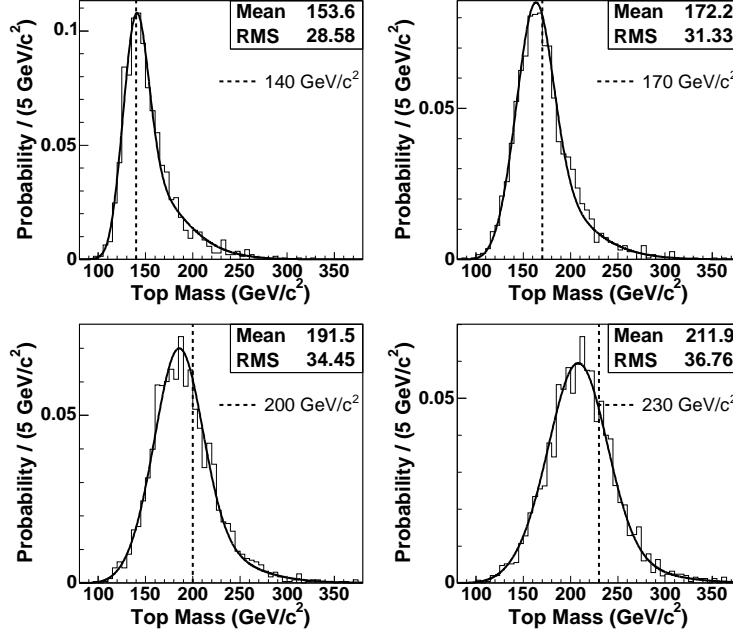


FIG. 8: Example signal templates as a function of the reconstructed top quark mass, from the PHI method applied to simulated signal samples at top quark masses of 140, 160, 190 and 220 GeV/c^2 . Overlaid are the parameterized fitting functions using Eq. 23. The vertical line indicates the generated top quark mass.

the integrals:

$$I_1 = \int_{90}^{300} e^{-\frac{1}{2}(\lambda_{\text{Landau}} + e^{-\lambda_{\text{Landau}}})} dm, \quad (28)$$

$$I_2 = \int_{90}^{300} e^{-\frac{1}{2}\lambda_{\text{Gauss}}^2} dm. \quad (29)$$

The parameters α_i ($i = 1, 5$) are simultaneously fit to all templates by assuming a linear dependence on the true top quark mass m_t :

$$\alpha_i(m_t) = a_i + b_i * m_t. \quad (30)$$

Example signal templates using the KIN method parameterization are shown in Fig. 9. We observe that, for all template methods, the mean of the signal template lies above the generated top quark mass for the $m_t = 140 \text{ GeV}/c^2$ sample, but moves below the generated value for higher mass samples.

For the background events, we create one representative background template by adding the individual templates from each background source according to their expected yields from

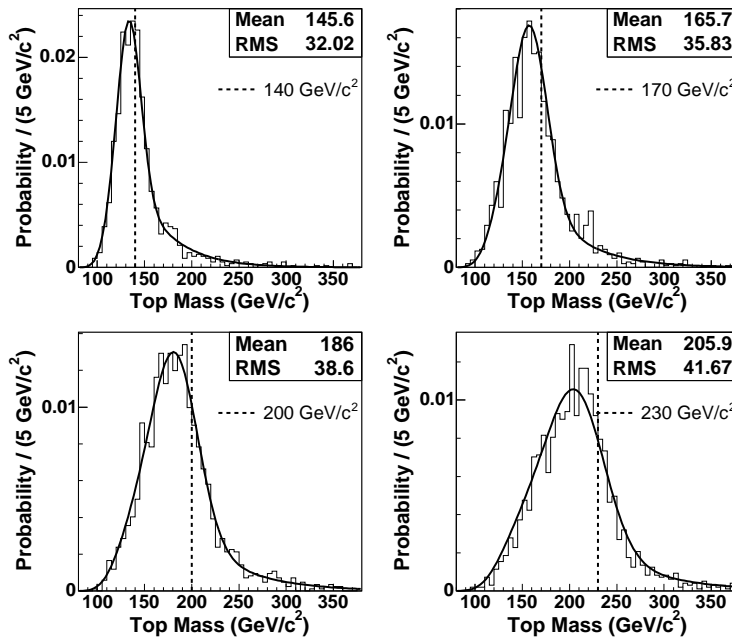


FIG. 9: Example signal templates as a function of the reconstructed top quark mass, from the KIN method applied to simulated signal samples at top quark masses of 130, 160, 190 and 220 GeV/c^2 . Overlaid are the parameterized fitting functions using Eq. 27. The vertical line indicates the generated top quark mass.

Table I. The templates from the various background processes are reconstructed from fully simulated Monte Carlo samples: the Drell-Yan events from PYTHIA, the $W(\rightarrow \ell\nu)$ +jets fakes from ALPGEN+HERWIG simulation of $W(\rightarrow e\nu) + 3$ partons, and the diboson from PYTHIA and ALPGEN+HERWIG. In combining these sources for each mass measurement technique, the measured efficiencies for finding a mass solution for each simulated background source are taken into account. We obtain the background p.d.f. ($P_b(m)$) by fitting the combined background template with a functional form identical to that used for the signal templates (Eq. 23 for the NWA and PHI methods, and Eq. 27 for the KIN method), but with fitted parameters independent of true top quark mass m_t . The resulting mass templates for the three background sources, along with the combined background template and parameterized fit, are plotted for each method in Figs. 10-12.

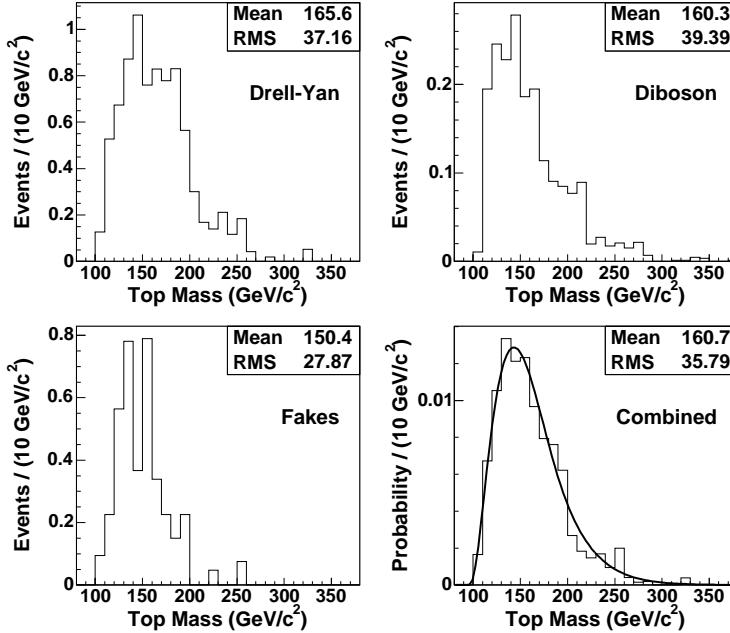


FIG. 10: Reconstructed top quark mass templates for the Drell-Yan, Diboson, and Fakes background sources using the NWA method, along with the combined background template and associated fitted probability density function. Background sources are normalized to the expected contribution in the 360 pb^{-1} LTRK sample.

B. Likelihood minimization

The final step for each dilepton template analysis is the determination of a representative top quark mass from the data sample by performing a likelihood fit and minimization. The likelihood function finds the probability that our data are described by an admixture of background events and dilepton $t\bar{t}$ decays with a certain top quark mass. As input we use the top quark mass values returned by the particular mass measurement technique applied to the data sample, and the parameterized probability density functions of the signal and background templates derived from simulation.

The total likelihood takes the form:

$$\mathcal{L}(m_t) = \mathcal{L}_{\text{shape}}(m_t) \times \mathcal{L}_{n_b} \quad (31)$$

where,

$$\mathcal{L}_{\text{shape}}(m_t) = \frac{e^{-(n_s+n_b)}(n_s+n_b)^N}{N!} \prod_{i=1}^N \frac{n_s P_s(m_i; m_t) + n_b P_b(m_i)}{n_s + n_b} \quad (32)$$

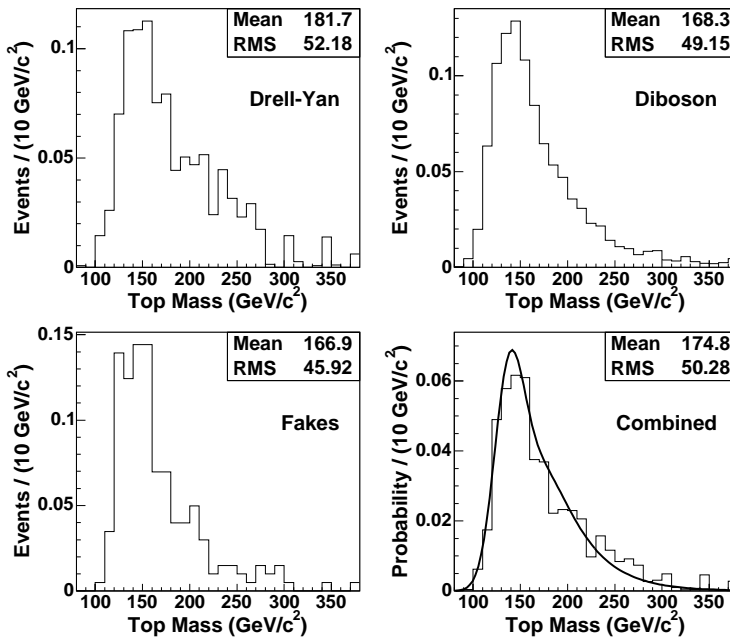


FIG. 11: Reconstructed top quark mass templates for the Drell-Yan, Diboson, and Fakes background sources using the KIN method, along with the combined background template and associated fitted probability density function. Background sources are normalized to the expected contribution in the 340 pb^{-1} DIL sample.

and

$$-\ln \mathcal{L}_{n_b} = \frac{(n_b - n_b^{\text{exp}})^2}{2\sigma_{n_b}^2}. \quad (33)$$

The likelihood returns a true top quark mass hypothesis (m_t), and estimated numbers of signal (n_s) and background (n_b) events. We assign a probability that each event (i) looks like signal and a probability that it looks like background. The signal and background probabilities are assigned by comparing the measured top quark mass values m_i from the data with the parameterized signal and background p.d.f.'s P_s and P_b . We find the probabilities that the likelihood-estimate for the number of background events n_b is consistent with our *a priori* estimate n_b^{exp} , and that the likelihood-estimate for the total number of signal (n_s) and background events is consistent with the observed number of events N . The number of background events is constrained with a Gaussian about n_b^{exp} (of width equal to the expected background uncertainty σ_{n_b}), while the sum of n_s and n_b is constrained with a Poisson term. In this manner, the likelihood-estimated number of signal events is independent of

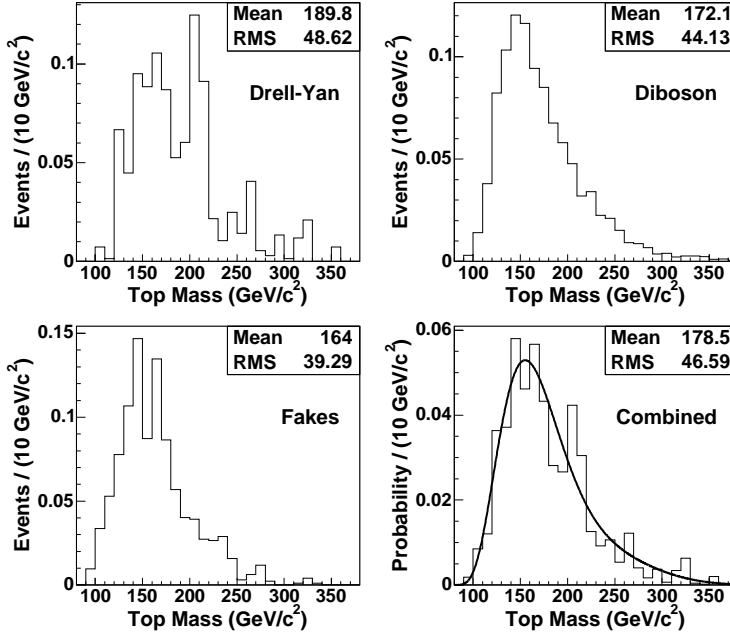


FIG. 12: Reconstructed top quark mass templates for the Drell-Yan, Diboson, and Fakes background sources using the PHI method, along with the combined background template and associated fitted probability density function. Background sources are normalized to the expected contribution in the 340 pb^{-1} DIL sample.

the expected number of signal events based on an assumed $t\bar{t}$ cross section. The true top quark mass hypothesis (m_t) which minimizes $-\ln(\mathcal{L})$ is retained.

The statistical uncertainty on m_t is given by the difference between the minimization mass result and the mass at $-\ln(\mathcal{L}/\mathcal{L}_{\max}) + 0.5$. In the NWA and KIN analyses, uncertainty on the top quark mass from uncertainties in the signal and background template parameterizations (due to limited statistics of the simulated template samples) is estimated and included as a systematic uncertainty (see Section VII). The PHI analysis incorporates this parameterization uncertainty directly into the top quark mass statistical uncertainty through the addition of a third term to the likelihood function (Eq. 31):

$$\mathcal{L}_{\text{param}} = \exp\left(-0.5\{(\vec{\alpha} - \vec{\alpha}_0)^T U^{-1}(\vec{\alpha} - \vec{\alpha}_0) + (\vec{\beta} - \vec{\beta}_0)^T V^{-1}(\vec{\beta} - \vec{\beta}_0)\}\right) \quad (34)$$

where U and V represent the covariance matrices of the signal and background parameters $\vec{\alpha}$ and $\vec{\beta}$, respectively.

V. TESTING WITH PSEUDO-EXPERIMENTS

We use a large number of simulated data ensembles, or pseudo-experiments, to check whether the methods for mass measurement described above return the expected top quark mass. For each generated top quark mass from 150 to 210 GeV/ c^2 , we construct a set of pseudo-experiments. Each pseudo-experiment consists of masses drawn randomly from the signal and background mass templates (*e.g.*, Figs. 7 and 10). The numbers of signal and background events in each pseudo-experiment are given by random Poisson fluctuations around the *a priori* estimates from the DIL and LTRK selections (see Table II). These estimates correspond to a $t\bar{t}$ cross section of 6.1 pb, and are adjusted for the reconstruction efficiency of each method for finding top quark mass solutions for signal and background events. The likelihood minimization procedure described in the previous section provides a “measured” top quark mass and statistical uncertainty for each pseudo-experiment. Figures 13-15 show the results from these pseudo-experiments for the NWA, KIN, and PHI methods, respectively. The upper plots show that the measured output top quark mass tracks the generated input mass. From the lower plots we observe that the residual differences between input and output top quark mass are consistent with zero for all methods, within uncertainties due to the limited statistics of the signal and background mass templates.

In order to check the consistency between the spread in output top quark mass and the estimated positive (σ_+) and negative (σ_-) statistical uncertainties from the pseudo-

TABLE II: Expected signal and background events for the NWA, KIN, and PHI methods applied to the LTRK (360 pb $^{-1}$) or DIL (340 pb $^{-1}$) selections, and corresponding to a $t\bar{t}$ cross section of 6.1 pb. Event numbers are adjusted for signal and background reconstruction efficiencies (in parentheses). Also shown is the *a priori* statistical uncertainty on top mass for each method using the $m_t = 178$ GeV/ c^2 simulation sample and correcting for underestimation found in pulls (by the scale in parentheses).

method	luminosity	expected sig.	expected bkg.	expected σ_{stat}
NWA	360 pb $^{-1}$	19.4 \pm 1.4 (99.8%)	14.1 \pm 3.5 (96%)	12.8 GeV/ c^2 (1.060)
KIN	340 pb $^{-1}$	12.9 \pm 1.1 (75%)	6.4 \pm 1.2 (61%)	15.1 GeV/ c^2 (1.033)
PHI	340 pb $^{-1}$	17.2 \pm 1.4 (100%)	10.5 \pm 1.9 (100%)	14.5 GeV/ c^2 (1.055)

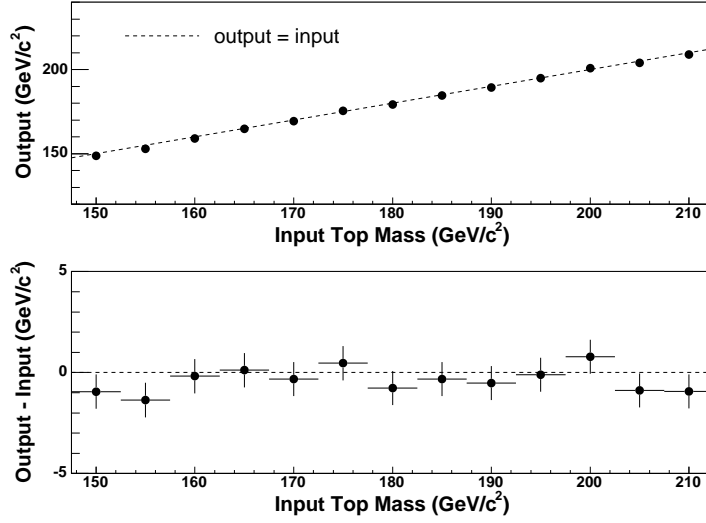


FIG. 13: Results from pseudo-experiment tests of the NWA method. The upper plot shows the mean of the output (measured) top quark mass as a function of the input (generated) mass, while the lower plot gives the difference between output and input top quark mass as a function of the input mass.

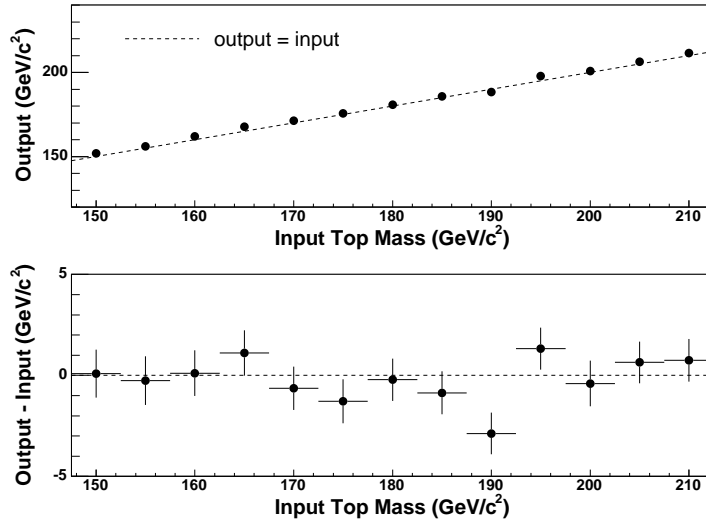


FIG. 14: Results from pseudo-experiment tests of the KIN method. The upper plot shows the mean of the output (measured) top quark mass as a function of the input (generated) mass, while the lower plot gives the difference between output and input top quark mass as a function of the input mass.

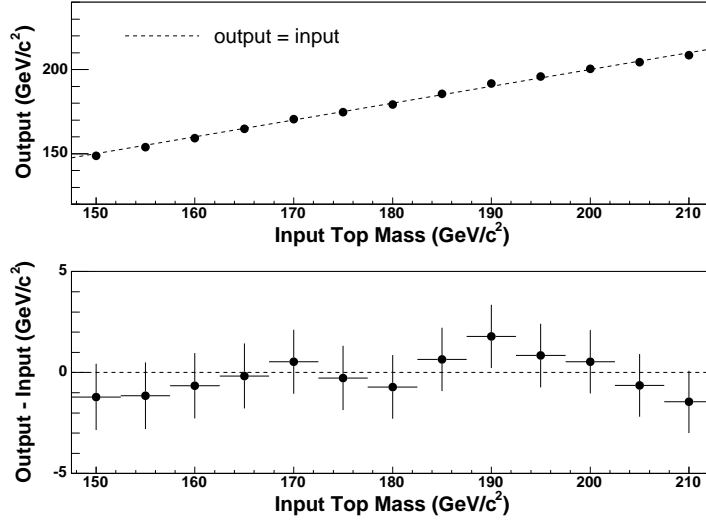


FIG. 15: Results from pseudo-experiment tests of the PHI method. The upper plot shows the mean of the output (measured) top quark mass as a function of the input (generated) mass, while the lower plot gives the difference between output and input top quark mass as a function of the input mass.

experiments, pull distributions are generated according to:

$$pull \equiv \frac{m_{\text{out}} - m_{\text{in}}}{(\sigma_+ + \sigma_-)/2} \quad (35)$$

for each of the generated samples at different input mass (with examples shown in Fig. 16). Figures 17-19 summarize the pull mean and width for the NWA, KIN, and PHI methods as a function of generated top quark mass, with corresponding uncertainties due to mass template statistics. Non-unity widths of the pull distributions indicate that the statistical uncertainty is underestimated for the three analyses. Therefore, we scale the uncertainties obtained from the likelihood fit on the data by the underestimation determined from the pseudo-experiments. Using the $m_t = 178 \text{ GeV}/c^2$ HERWIG simulation and assuming a $t\bar{t}$ cross section of 6.1 pb, Table II compares the expected statistical uncertainty of the three measurement techniques after applying this correction due to observed pull width (shown in parentheses).

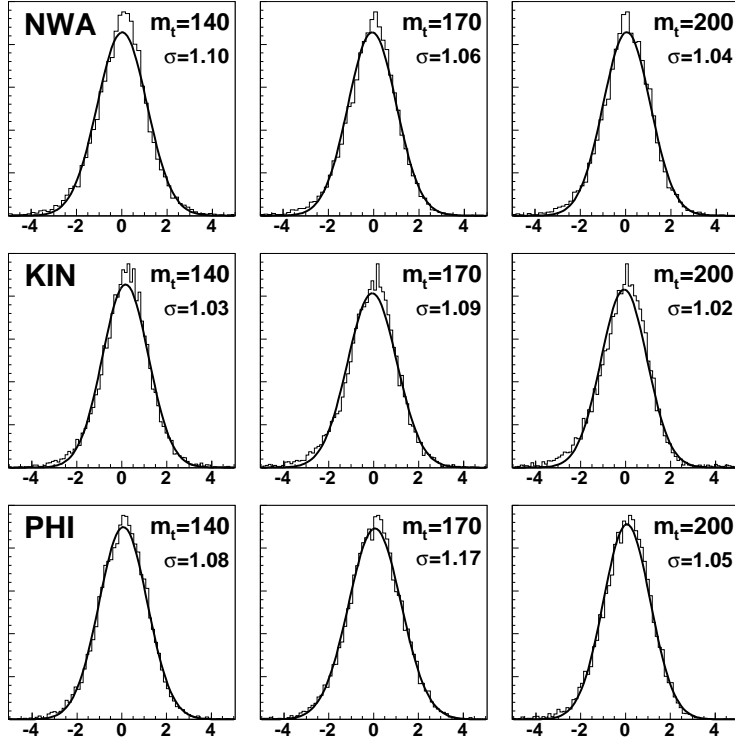


FIG. 16: Example pull distributions for the NWA (upper), KIN (middle), and PHI (lower) pseudo-experiments, corresponding to generated mass samples at 140, 170, and 200 GeV/c^2 . Each pull distribution is fit to a Gaussian (solid line), with noted standard deviation (σ).

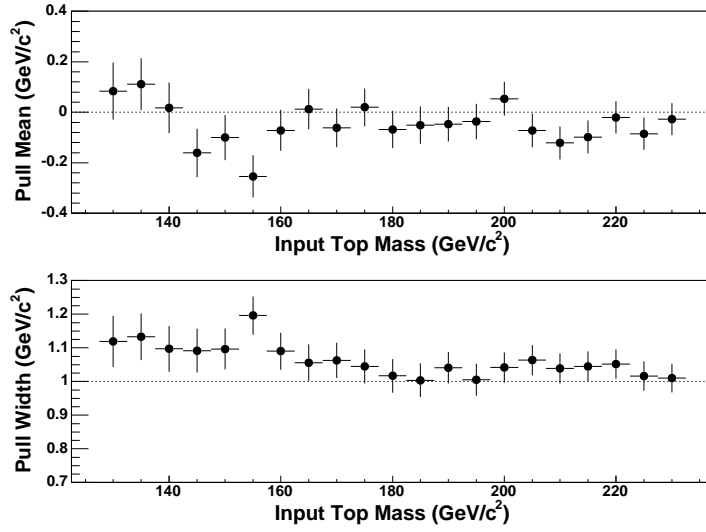


FIG. 17: Summary of pull distributions for the NWA pseudo-experiments, showing the pull mean (upper) and width (lower) as a function of generated input top quark mass, compared with zero mean and unity width (horizontal lines).

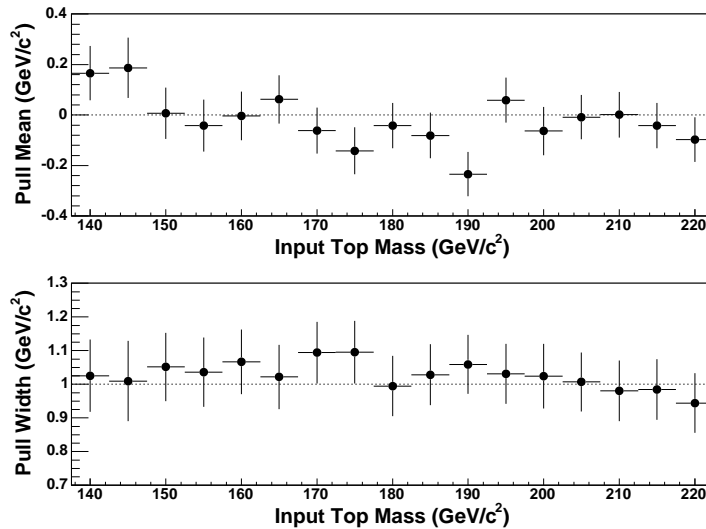


FIG. 18: Summary of pull distributions for the KIN pseudo-experiments, showing the pull mean (upper) and width (lower) as a function of generated input top quark mass, compared with zero mean and unity width (horizontal lines).

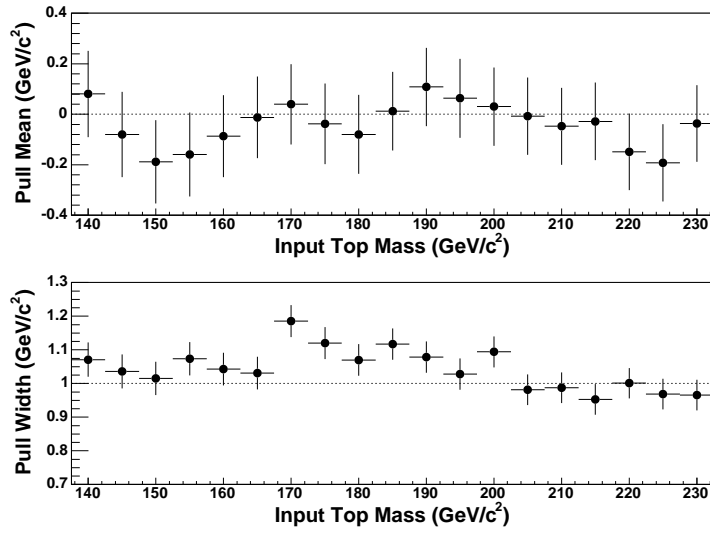


FIG. 19: Summary of pull distributions for the PHI pseudo-experiments, showing the pull mean (upper) and width (lower) as a function of generated input top quark mass, compared with zero mean and unity width (horizontal lines).

VI. RESULTS

The NWA procedure is applied to the 46 events satisfying the LTRK selection in 360 pb^{-1} of Run II data, with 45 events resulting in NWA solutions. The KIN and PHI analyses are applied to the 33 events of the DIL selection sample, corresponding to 340 pb^{-1} . Of this sample, 30 events pass kinematic reconstruction in the KIN method, while the PHI analysis returns solutions for all 33 events. Each method applies the likelihood procedure described in Sec. IV, using the expected number of background events listed in Table II for the LTRK or DIL selection sample after accounting for mass reconstruction efficiency. As listed in Table III, each likelihood fit returns a constrained number of background events consistent with the expected value. The number of signal events returned from each likelihood fit ensures that the total number of events in the likelihood agrees with that observed, thereby accounting for the upward fluctuations in both the DIL and LTRK selection samples.

The upper plots of Figs. 20-22 show for the NWA, KIN, and PHI methods, respectively, the reconstructed top quark mass in the data, the normalized background and signal+background shapes, and the variation of $-\ln(\mathcal{L}/\mathcal{L}_{\max})$ as a function of the top quark mass hypothesis. For each method, the final top quark mass is taken as the value of m_t which minimizes the likelihood function. Statistical uncertainties are obtained by taking the width at $-\ln(\mathcal{L}/\mathcal{L}_{\max})+0.5$, and adjusting for the underestimation found in pull widths from Figs. 17-19. Table III summarizes the measured top quark mass and statistical uncertainty

TABLE III: Summary of results for the NWA, KIN, and PHI methods applied to the LTRK and DIL data samples. Listed for each method are: number of total observed events in the sample, number of events with mass solutions, expected number of background events, constrained likelihood fit values for signal and background events and top quark mass, and unconstrained likelihood mass.

method	data sample			constrained results			unconstrained
	N_{tot}	N_{sol}	n_b^{exp}	n_s	n_b	$m_t \text{ (GeV}/c^2)$	$m_t \text{ (GeV}/c^2)$
NWA	46	45	14.1 ± 3.5	32.4 ± 7.4	13.4 ± 3.5	$170.7^{+6.9}_{-6.5}$	168.3 ± 4.9
KIN	33	30	6.4 ± 1.2	24.5 ± 5.6	6.1 ± 1.7	$169.5^{+7.7}_{-7.2}$	168.4 ± 6.1
PHI	33	33	10.5 ± 1.9	24.4 ± 5.9	10.0 ± 1.9	$169.7^{+8.9}_{-9.0}$	169.2 ± 6.4

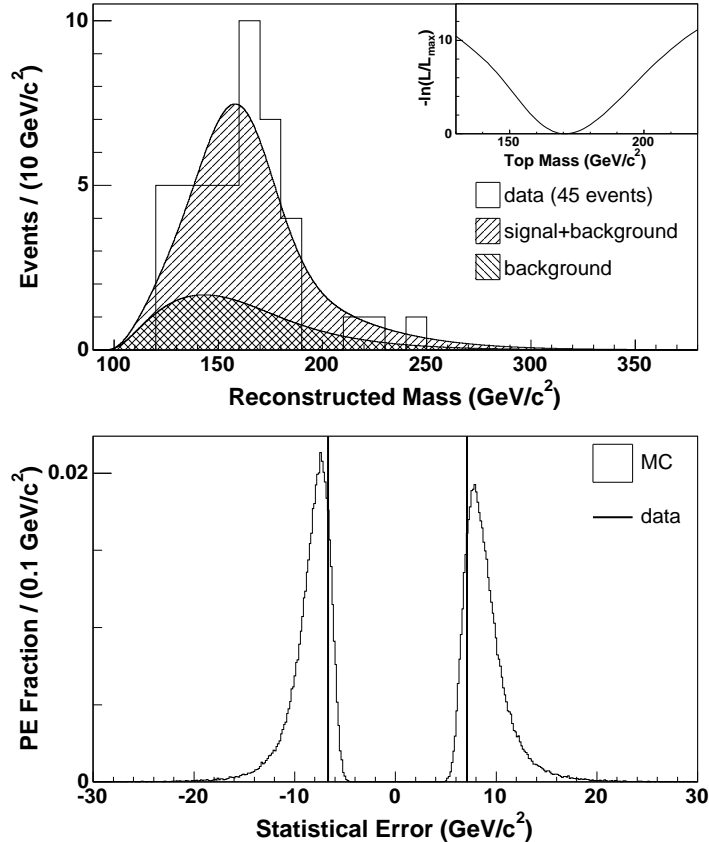


FIG. 20: Results for the NWA method applied to the 46-event LTRK data sample, leading to 45 solutions. Upper plot: reconstructed top quark mass for the data events (histogram), with normalized background and signal+background p.d.f. curves, and the likelihood function (inset). Lower plot: comparison of measured positive and negative statistical uncertainties in the data sample (vertical lines) with pseudo-experiments generated using the $170 \text{ GeV}/c^2$ signal template and assuming at least 45 events observed.

for the three mass methods after pull width corrections.

The lower plots of Figs. 20-22 compare the measured statistical uncertainties of the NWA, KIN, and PHI methods with pseudo-experiments using the $m_t = 170 \text{ GeV}/c^2$ sample which have the same number of events as that observed in the data for each method. We find the probabilities for achieving the observed statistical uncertainties to be 9%, 23%, and 19% for the NWA, KIN, and PHI methods, respectively. As a further cross-check, we remove the Gaussian constraint on the number of background events in the likelihood procedure (*i.e.*, the term \mathcal{L}_{n_b} in Eq. 31). For all three methods, this unconstrained fit converges near

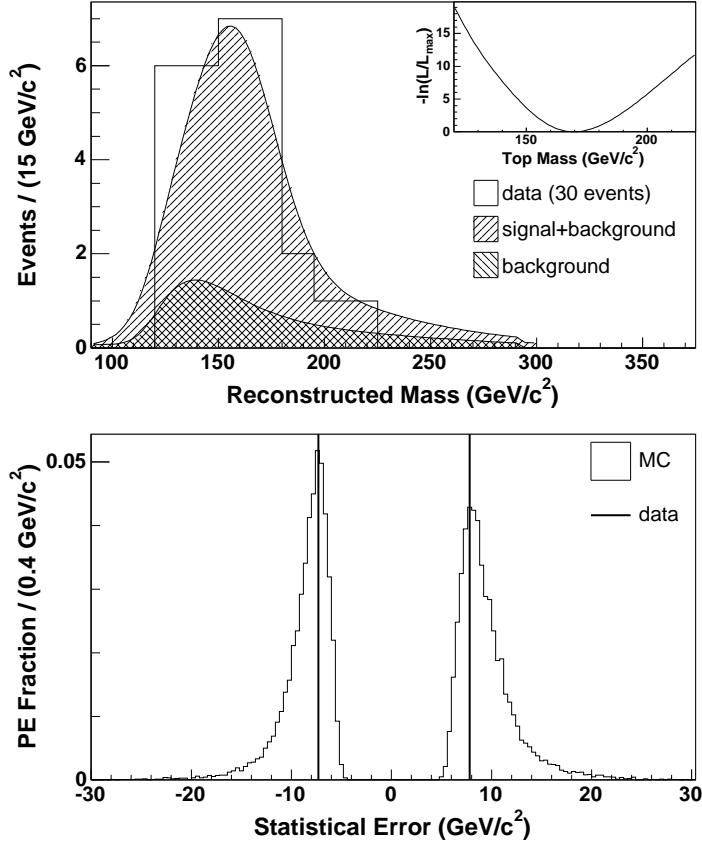


FIG. 21: Results for the KIN method applied to the 33-event DIL data sample, leading to 30 solutions. Upper plot: reconstructed top quark mass for the data events (histogram), with normalized background and signal+background p.d.f. curves, and the likelihood function (inset). Lower plot: comparison of measured average statistical uncertainty in the data sample (vertical line) with pseudo-experiments generated using the $170 \text{ GeV}/c^2$ signal template.

zero background events, which is found to occur for 21% (NWA), 31% (KIN), and 20% (PHI) of pseudo-experiments using the $m_t = 170 \text{ GeV}/c^2$ sample. The resulting top quark mass of the unconstrained fit, corrected for pull width, is consistent with the constrained result for each mass method (as seen in Table III). The statistical uncertainty returned by the unconstrained fit on the data sample is smaller than that of the constrained fit for all methods. However, from studies of pseudo-experiments at $m_t = 170 \text{ GeV}/c^2$ we expect on average an improvement in statistical uncertainty of 1.1, 1.5, and 1.2 GeV/c^2 for the NWA, KIN, and PHI methods, respectively, when applying the background constraint to the likelihood function.

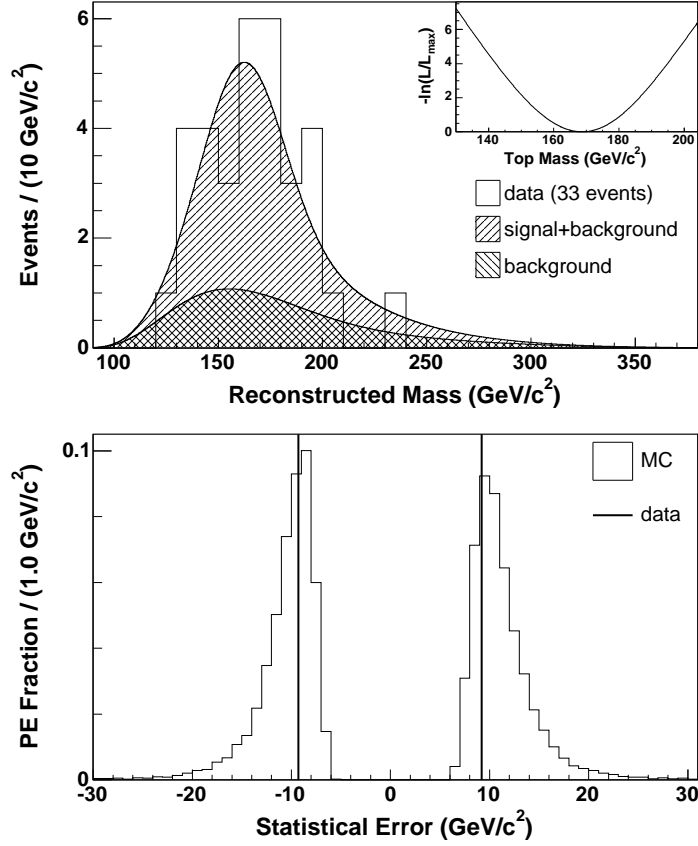


FIG. 22: Results for the PHI method applied to the 33-event DIL data sample. Upper plot: reconstructed top quark mass for the data events (histogram), with normalized background and signal+background p.d.f. curves, and the likelihood function (inset). Lower plot: comparison of measured positive and negative statistical uncertainties in the data sample (vertical lines) with pseudo-experiments generated using the 170 GeV/c² signal template.

VII. SYSTEMATIC UNCERTAINTIES

Apart from the statistical uncertainty on the measured top quark mass due to the limited size of our data sample, there are several sources of systematic uncertainty. These systematic effects stem from uncertainty in the Monte Carlo simulation of $t\bar{t}$ and background events, from mismodeling by the simulation of the detector response to leptons and jets, and from the validity of various assumptions made during the implementation of the mass measurement techniques. As such, most sources of systematic uncertainty are common to all three mass analyses, and are estimated by adjusting a particular input value to the simulation and constructing new mass templates. We then perform pseudo-experiments using events drawn from the new mass templates, and compare the resulting median reconstructed top quark mass with that of the nominal simulation. The sources of systematic uncertainty within each mass analysis are assumed to be uncorrelated, so that a total systematic uncertainty for each method is calculated as the sum in quadrature of the various sources, as summarized in Table IV.

One of the largest sources of systematic uncertainty arises from potential mismodeling of the jet energy measurement, through uncertainties in the various corrections applied to the measured jet energy [14]. These jet energy corrections involve the non-uniformity in response of the calorimeter as a function of η , effects from multiple $p\bar{p}$ collisions, the absolute jet energy scale for hadrons, energy deposition from the underlying $p\bar{p}$ event, and energy loss outside the jet search cone ΔR . A systematic uncertainty is estimated for each jet energy correction by performing pseudo-experiments drawn from signal and background templates with ± 1 standard deviation in correction uncertainty, and taking the half-difference in median reconstructed top quark mass between the two results. The uncertainties from each energy correction are then added in quadrature to arrive at a total systematic uncertainty on the jet energy scale.

Since the above jet energy corrections are developed from studies of samples dominated by light-quark and gluon jets, additional uncertainty occurs from extrapolating this procedure to b -quarks. The resulting systematic effect on jet energy is considered to stem from three main sources: uncertainty in the b -jet fragmentation model, differences in the energy response due to semi-leptonic decays of b -hadrons, and uncertainty in the color flow within top quark production and decay to b -jets [25]. As in the jet energy scale uncertainty,

pseudo-experiments are performed on events where the b -jet energies have been altered by ± 1 standard deviation for each uncertainty, and the resulting half-differences added in quadrature to estimate the total systematic uncertainty due to b -jet energy uncertainty.

Several systematic uncertainties are due to the modeling of the $t\bar{t}$ signal. We study the effects of the particular Monte Carlo generator chosen by comparing pseudo-experiments drawn from **PYTHIA** simulation with events taken from our nominal signal templates constructed using **HERWIG**. These generators differ in their hadronization models and in their handling of the underlying $p\bar{p}$ event and multiple $p\bar{p}$ interactions [26]. We take the difference in reconstructed top quark mass between **HERWIG** and **PYTHIA** pseudo-experiments as the systematic uncertainty due to choice of generator. The systematic uncertainty associated with the initial state radiation (ISR) is studied by changing the QCD parameters for parton shower evolution according to comparisons between CDF Drell-Yan data and simulation [25]. Since final state radiation (FSR) shares the same Monte Carlo shower algorithms as ISR, these variations in QCD parameters are used to generate FSR systematic samples by varying a set of parameters specific to FSR modeling. We then compare the reconstructed top quark mass from samples with increased and decreased ISR and FSR to estimate the systematic uncertainty due to these sources. The uncertainty in reconstructed top quark mass from our choice of parton distribution function (PDF) is found by comparing two different groups (**CTEQ5L** [19] and **MRST72** [27]). Additionally, **MRST72** and **MRST75** sets, derived using different Λ_{QCD} values, are compared, and 20 eigenvectors within the **CTEQ6M** group are varied by ± 1 standard deviation. Differences in pseudo-experiment results from these variations are added in quadrature to arrive at a total systematic uncertainty from the choice of PDF. Further studies comparing LO with NLO $t\bar{t}$ Monte Carlo show a negligible effect on the reconstructed top quark mass.

Since our background template is also derived from simulation, another source of systematic uncertainty reflects the potential mismodeling by the Monte Carlo of the background shape. Background events may pass event selection through processes which are not accurately modeled in the simulation, such as tracks or jets passing through gaps in detector elements. This uncertainty is estimated by measuring the resulting top quark mass from pseudo-experiments where the track p_T , jet energy, and \cancel{E}_T of each background sample have been altered by the measured discrepancies in these quantities between simulation and data. Another systematic uncertainty affecting the background shape is due to uncertainty

in the relative composition of the background sources used to construct the total background template. To estimate this uncertainty, we measure the effect on top quark mass from pseudo-experiments where the relative combination of Drell-Yan and fake backgrounds (the largest two sources) is adjusted by predicted uncertainty.

The finite statistics in the simulated signal and background templates result in a systematic uncertainty on the parameterized p.d.f.'s used in the likelihood (Eq. 32), even if modeling of the signal and background processes is correct. As described in Section IV, the PHI method accounts for this uncertainty in template parameterizations within the statistical uncertainty returned by the likelihood minimization through the term $\mathcal{L}_{\text{param}}$ of Eq. 34. The NWA and KIN procedures estimate directly the top quark mass uncertainty due to finite template statistics, and incorporate this effect into the total systematic uncertainty. For each signal template, we Poisson fluctuate the number of events in each bin to create a new template, which is parameterized according to Eqs. 23 and 27. We then perform pseudo-experiments drawing signal events from the nominal templates but applying them to a likelihood fit with the fluctuated signal p.d.f. in Eq. 32, producing a distribution of reconstructed top quark mass. Repeating this procedure many times, we estimate the systematic uncertainty due to limited statistics in the signal templates as the root mean square of the median reconstructed top quark masses from the fluctuated pseudo-experiments. In a similar fashion, we estimate the analogous systematic uncertainty due to limited background template statistics by fluctuating each template bin of the various background components.

TABLE IV: Summary of the systematic uncertainties on the top quark mass measurement (in GeV/c^2) for the NWA, KIN, and PHI analyses. The total uncertainty is obtained by adding the individual contributions in quadrature. (The uncertainty due to signal and background template statistics for the PHI method is accounted for in the total statistical uncertainty).

systematic source	NWA	KIN	PHI
Jet energy scale	3.4	3.2	3.5
b -jet energy	0.6	0.6	0.7
MC generator	0.5	0.6	0.7
PDF's	0.5	0.5	0.6
ISR	0.6	0.6	0.6
FSR	0.5	0.3	0.4
Background shape	2.6	1.6	1.5
Template statistics			
Signal	0.2	0.4	n/a
Background	1.3	1.2	n/a
Total	4.6	4.0	4.0

VIII. COMBINATION OF MEASUREMENTS

Table V shows the results, including statistical and systematic uncertainties, for the NWA, KIN, and PHI analyses. The three results are consistent, and can be combined to improve upon the overall precision of the top quark mass measurements using the template method. The combination procedure follows the Best Linear Unbiased Estimation (BLUE) method [28]. In this technique, the final result consists of a linear combination of the individual measurements. The measured statistical and systematic uncertainties for each measurement, along with their correlations, are used to construct an error matrix, which upon inversion gives the corresponding weights for each method within the combined result.

The statistical correlations between methods are determined from simulated samples over a range of top quark masses from 155 to 195 GeV/ c^2 . Pseudo-experiments from these samples, each corresponding to an integrated luminosity of 350 pb $^{-1}$, are constructed. The LTRK and DIL selection criteria are applied to the pseudo-experiments to model the expected signal sample, as well as correlations between the selection methods. Simulated background events are added to each pseudo-experiment according to the expected contributions to each selection from the three background sources (as listed in Table I). Based on studies from simulation, the $W(\rightarrow \ell\nu)$ +jets fake background is assumed to be uncorrelated between the DIL and LTRK selections. For the diboson and Drell-Yan DIL backgrounds, a Poisson fluctuated number of events with mean $\langle N_{\text{DIL}} \rangle$ is added to each pseudo-experiment, drawn from a pool of events passing the DIL selection. The LTRK diboson and Drell-Yan backgrounds are constructed by taking into account the expected number of common events, $N_{\text{LTRK}\cdot\text{DIL}}$, between the two selections, as determined from simulation. These LTRK backgrounds are thus the union of $N_{\text{LTRK}\cdot\text{DIL}}$ common events with a number of events $\langle N_{\text{LTRK}} - N_{\text{LTRK}\cdot\text{DIL}} \rangle$ drawn from the pool of those events passing only the LTRK selection. From these pseudo-experiments of signal and background events, we find an overlap between the LTRK and DIL selections of approximately 30%, compared with the 44% overlap observed in the two data samples.

The three measurement methods are applied to each pseudo-experiment, returning a reconstructed top quark mass and expected statistical uncertainty. Pseudo-experiments where the likelihood minimization for any of the methods fails to converge are removed from consideration. This situation occurs for approximately 0.8% of all pseudo-experiments. Also,

pseudo-experiments must have a returned mass which lies within the likelihood minimization mass range of all methods. The correlation coefficient between two mass measurements m_i and m_j is calculated from the N pseudo-experiments at each mass sample by the equation:

$$\rho_{ij} = \frac{N \sum m_i m_j - \sum m_i \sum m_j}{\sqrt{N \sum m_i^2 - (\sum m_i)^2} \sqrt{N \sum m_j^2 - (\sum m_j)^2}}. \quad (36)$$

These statistical correlations are shown in Table V for the $m_t = 170 \text{ GeV}/c^2$ sample, and are stable across the 155 to 195 GeV/c^2 mass samples. Systematic uncertainties common to all three methods, as listed in Table IV, are assumed to be 100% correlated, while the systematic uncertainties due to limited template statistics for the NWA and KIN methods are assumed to be uncorrelated. After incorporating systematic effects, Table V shows the total correlations between methods in parentheses, and the resulting weights of the methods after inversion of the constructed error matrix.

Since measurements producing smaller mass values tend to have correspondingly smaller statistical uncertainties, an iterative combination procedure is performed in order to prevent bias towards lower mass values. In this procedure, each measurement method is assumed to have a constant fractional statistical uncertainty (taken from the expected uncertainty at $m_t = 178 \text{ GeV}/c^2$ in Table II). Combining the three measurements, each method's statistical uncertainty is then extrapolated to the combination value, and the procedure repeated until the combined result converges.

Potential bias in the combination technique is studied by using the pseudo-experiment results from each method as input. As shown in Fig. 23, we observe no bias in the residual difference between the input and output top quark mass of the combination result for samples above $m_t = 160 \text{ GeV}/c^2$. However, non-unity pull widths for all mass samples indicate that the statistical uncertainty of the combination procedure is slightly underestimated. Studies of toy Monte Carlo pseudo-experiments suggest that this underestimation may stem from deviations in the data sample from assumptions made in the BLUE method (*e.g.*, Gaussian uncertainties). Applying the combination procedure to the NWA, KIN, and PHI data sample measurements, and correcting the returned statistical uncertainty by the average pull width over all mass samples (a scale factor of 1.15), yields a top quark mass of 170.1 ± 6.0 (stat.) ± 4.1 (syst.) GeV/c^2 . The close proximity of the three template measurements with respect to their measured uncertainties leads to a χ^2 per degrees of freedom for the combination of $\chi^2/\text{d.o.f.} = 0.017/2$, corresponding to a p -value of 99%.

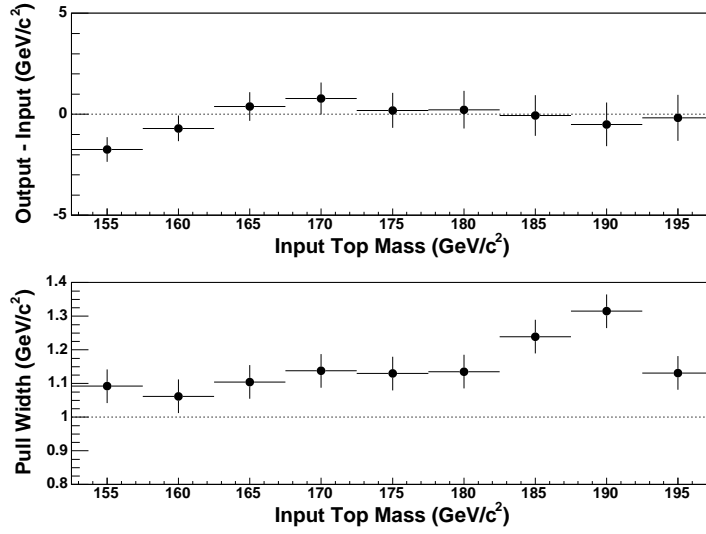


FIG. 23: Summary of the difference between output and input top quark mass (upper) and width of pull distributions (lower) for the combination pseudo-experiments, as a function of generated input top quark mass.

TABLE V: Summary of measured top quark masses for the Neutrino Weighting Algorithm (NWA), Full Kinematic Analysis (KIN), and Neutrino ϕ Weighting Method (PHI), along with their statistical (total) correlations, and contributing weight to the combined top quark mass result.

method	result (GeV/c ²)	correlation			weight
		NWA	KIN	PHI	
NWA	$170.7^{+6.9}_{-6.5}$ (stat.) \pm 4.6 (syst.)	1.00 (1.00)	0.14 (0.32)	0.25 (0.40)	47%
KIN	$169.5^{+7.7}_{-7.2}$ (stat.) \pm 4.0 (syst.)		1.00 (1.00)	0.35 (0.46)	38%
PHI	$169.7^{+8.9}_{-9.0}$ (stat.) \pm 4.0 (syst.)			1.00 (1.00)	15%

IX. SUMMARY

We have performed three separate measurements of the top quark mass from $t\bar{t}$ events produced in $p\bar{p}$ collisions at a center-of-mass energy of 1.96 TeV, using the Run II Collider Detector at Fermilab. The mass measurements employ one of two complementary selection algorithms to extract $t\bar{t}$ events where both W bosons from the top quarks decay into leptons ($e\nu, \mu\nu, \text{ or } \tau\nu$), producing data samples of 340 and 360 pb^{-1} . Each measurement technique determines a single top quark mass for an event by making different assumptions in order to resolve the underconstrained dilepton $t\bar{t}$ decays. For each method, template mass distributions are constructed from simulated signal and background processes, and parameterized to form continuous probability density functions. A likelihood fit incorporating these parameterized templates is then performed on the data sample masses in order to derive a final top quark mass.

One method, the Neutrino Weighting Algorithm (NWA), measures a top quark mass of $170.7_{-6.5}^{+6.9}$ (stat.) ± 4.6 (syst.) GeV/c^2 . A second technique, called the Full Kinematic Analysis (KIN), results in a mass measurement of $169.5_{-7.2}^{+7.7}$ (stat.) ± 4.0 (syst.) GeV/c^2 . A third analysis using the Neutrino ϕ Weighting Method (PHI) measures a value of $169.7_{-9.0}^{+8.9}$ (stat.) ± 4.0 (syst.) GeV/c^2 . Accounting for correlations in the statistical and systematic uncertainties between methods, we combine the three results, giving a top quark mass in the dilepton channel of 170.1 ± 6.0 (stat.) ± 4.1 (syst.) GeV/c^2 . This combined result is consistent with the CDF Run II “lepton+jets” channel [29], which used a 318 pb^{-1} data sample to measure a top quark mass of $173.5_{-3.8}^{+3.9}$ GeV/c^2 , and thus gives no indication of new physics in the dilepton channel. The three template analyses are also consistent with a fourth CDF top quark mass measurement in the dilepton channel [30], which applies a matrix-element technique to the 33-event DIL selection sample.

Acknowledgments

We thank the Fermilab staff and the technical staffs of the participating institutions for their vital contributions. This work was supported by the U.S. Department of Energy and National Science Foundation; the Italian Istituto Nazionale di Fisica Nucleare; the Ministry of Education, Culture, Sports, Science and Technology of Japan; the Natural Sciences

and Engineering Research Council of Canada; the National Science Council of the Republic of China; the Swiss National Science Foundation; the A.P. Sloan Foundation; the Bundesministerium für Bildung und Forschung, Germany; the Korean Science and Engineering Foundation and the Korean Research Foundation; the Particle Physics and Astronomy Research Council and the Royal Society, UK; the Russian Foundation for Basic Research; the Comisión Interministerial de Ciencia y Tecnología, Spain; in part by the European Community's Human Potential Programme under contract HPRN-CT-2002-00292; and the Academy of Finland.

-
- [1] F. Abe *et al.* (CDF Collaboration), Phys. Rev. Lett. **74**, 2626 (1995); S. Abachi *et al.* (DØ Collaboration), Phys. Rev. Lett. **74**, 2632 (1995).
- [2] CDF and DØ Collaborations, and the Tevatron Electroweak Working Group, arXiv:hep-ex/0404010.
- [3] M. Hashimoto, M. Tanabashi and K. Yamawaki, Phys. Rev. D **64**, 056003 (2001); V.A. Miransky, M. Tanabashi and K. Yamawaki, Mod. Phys. Lett. A **4**, 1043 (1989).
- [4] Z.J. Xiao, J.Y. Zhang, L.D. Wan, X.L. Wang and G.R. Lu, J. Phys. G **21**, 19 (1995).
- [5] D. Acosta *et al.*, Phys. Rev. D **71**, 032001 (2005); The CDFII Detector Technical Design Report, Fermilab-Pub-96/390-E.
- [6] C.S. Hill, Nucl. Instrum. Methods A **530**, 1 (2004); A. Sill *et al.*, Nucl. Instrum. Methods A **447**, 1 (2000); A. Affolder *et al.*, Nucl. Instrum. Methods A **453**, 84 (2000).
- [7] T. Affolder *et al.*, Nucl. Instrum. Methods A **526**, 249 (2004).
- [8] M. Albrow *et al.*, Nucl. Instrum. Methods A **480**, 524-545 (2002); G. Apollinari *et al.*, Nucl. Instrum. Methods A **412**, 515-526 (1998).
- [9] L. Balka *et al.*, Nucl. Instrum. Methods A **267**, 272-279 (1988); S.R. Hahn *et al.*, Nucl. Instrum. Methods A **267**, 351-366 (1988); S. Bertolucci *et al.*, Nucl. Instrum. Methods A **267**, 301-314 (1988).
- [10] G. Ascoli *et al.*, Nucl. Instrum. Methods A **268**, 33 (1988); T. Dorigo *et al.*, Nucl. Instrum. Methods A **461**, 560 (2001).
- [11] D. Acosta *et al.*, Nucl. Instrum. Methods A **494**, 57 (2002).
- [12] D. Acosta *et al.* (CDF Collaboration), Phys. Rev. Lett. **93**, 142001-1 (2004).

- [13] F. Abe *et al.* (CDF Collaboration), Phys. Rev. Lett. **80**, 2779 (1998).
- [14] A. Bhatti *et al.*, arXiv:hep-ex/0510047.
- [15] T. Sjostrand *et al.*, Comp. Phys. Commun. **135**, 238 (2001).
- [16] M. Cacciari *et al.*, J. High Energy Phys. **404**, 068 (2004).
- [17] M.L. Mangano *et al.*, J. High Energy Phys. **307**, 001 (2003).
- [18] G. Corcella *et al.*, “HERWIG 6: An event generator for hadron emission reactions with interfering gluons (including supersymmetric processes),” JHEP **0101**, 010 (2001)
- [19] H.L. Lai *et al.*, Eur. Phys. J. **C12**, 375 (2000).
- [20] B. Abbott *et al.* (DØ Collaboration), Phys. Rev. D **60**, 052001 (1999).
- [21] F. Abe *et al.* (CDF Collaboration), Phys. Rev. Lett. **82**, 271 (1999); T. Affolder *et al.* (CDF Collaboration), Phys. Rev. D **63**, 032003 (2001).
- [22] D. Acosta *et al.* (CDF Collaboration), Phys. Rev. D **71**, 052003 (2005).
- [23] W. Press *et al.*, “Numerical Recipes in C: The Art of Scientific Computing,” Cambridge University Press (1992).
- [24] S. Eidelman *et al.* (Particle Data Group), Phys. Lett. B **592**, 1 (2004).
- [25] A. Abulencia *et al.* (CDF Collaboration), arXiv:hep-ex/0510048.
- [26] T. Sjostrand, Comp. Phys. Commun. **82**, 74 (1994); G. Marchesini *et al.*, Comp. Phys. Commun. **67**, 465 (1991).
- [27] A.D. Martin, R.G. Roberts, W.J. Stirling and R.S. Thorne, Eur. Phys. J. **C4**, 463 (1998).
Implementation from: PDFLIB: The Parton Density Functions Library, Version 8.04, MRST set 75, CERN.
- [28] L. Lyons, D. Gibaut and P. Clifford, Nucl. Instrum. Methods A **270**, 110-117 (1988);
A. Valassi, Nucl. Instrum. Methods A **500**, 391 (2003).
- [29] A. Abulencia *et al.* (CDF Collaboration), arXiv:hep-ex/0510049.
- [30] A. Abulencia *et al.* (CDF Collaboration), arXiv:hep-ex/0512070.